Bioactive Materials 46 (2025) 347–364

Contents lists available at ScienceDirect

Bioactive Materials

journal homepage: www.keaipublishing.com/en/journals/bioactive-materials

Fabrication and functional validation of a hybrid biomimetic nanovaccine (HBNV) against Kit^{K641E}-mutant melanoma

Kishwor Poudel [a], Zhenyu Ji [a], Ching-Ni Njauw [a], Anpuchchelvi Rajadurai [a], Brijesh Bhayana [a], Ryan J. Sullivan [b], Jong Oh Kim [c], Hensin Tsao [a,b,*]

[a] Wellman Center for Photomedicine and Department of Dermatology, Massachusetts General Hospital, Harvard Medical School, Boston, MA, USA
[b] Mass General Cancer Center, Massachusetts General Hospital, Harvard Medical School, Boston, MA, USA
[c] College of Pharmacy, Yeungnam University, Gyeongsan, 38541, Republic of Korea

ARTICLE INFO

Keywords:
Cancer vaccines
Immunotherapy
KIT-Mutant melanoma
Nanovaccines
Hybrid

ABSTRACT

Cancer nanovaccines hold the promise for personalization, precision, and pliability by integrating all the elements essential for effective immune stimulation. An effective immune response requires communication and interplay between antigen-presenting cells (APCs), tumor cells, and immune cells to stimulate, extend, and differentiate antigen-specific and non-specific anti-tumor immune cells. The versatility of nanomedicine can be adapted to deliver both immunoadjuvant payloads and antigens from the key players in immunity (i.e., APCs and tumor cells). The imperative for novel cancer medicine is particularly pressing for less common but more devastating KIT-mutated acral and mucosal melanomas that are resistant to small molecule c-kit and immune checkpoint inhibitors. To overcome this challenge, we successfully engineered nanotechnology-enabled hybrid biomimetic nanovaccine (HBNV) comprised of membrane proteins (antigens to activate immunity and homing/targeting ligand to tumor microenvironment (TME) and lymphoid organs) from fused cells (of APCs and tumor cells) and immunoadjuvant. These HBNVs are efficiently internalized to the target cells, assisted in the maturation of APCs via antigens and adjuvant, activated the release of anti-tumor cytokines/inhibited the release of immunosuppressive cytokine, showed a homotypic effect on TME and lymph nodes, activated the anti-tumor immune cells/downregulated the immunosuppressive immune cells, reprogram the tumor microenvironment, and showed successful anti-tumor therapeutic and prophylactic effects.

1. Introduction

KIT mutations in melanoma represent a rare but distinct clinical subset that is more prevalent among acral and mucosal melanomas (AM and MM, respectively). KIT alterations occur in up to 40 % of reported series of A.M.s and M.M.s [1–4]. These mutations, predominantly located in the juxtamembrane domain, confer a variable response to tyrosine kinase inhibitors (TKIs), with median progression-free survival (PFS) of less than 6 months [1,4]. A major challenge is the heterogeneity of KIT mutations, which affects the efficacy of TKIs, as not all mutations are equally sensitive to such therapies. Additionally, the rarity of KIT mutations in melanoma complicates the accumulation of robust clinical trial data and hinders the development of optimized treatment protocols tailored to this subgroup. Furthermore, resistance to targeted therapy often develops, necessitating the development of combination therapies or new agents capable of bypassing resistance mechanisms. Lastly, immune checkpoint inhibitors for AM and MM have also proven inadequate, with pooled analyses demonstrating a median PFS of only ~2–3 months [5]. Thus, managing KIT mutated melanomas, regardless of AM or MM, requires a nuanced understanding of molecular diagnostics, personalized treatment approaches, and ongoing research into more effective and durable therapeutic strategies.

Cancer vaccines exploit the immune system's capacity to recognize both tumor-associated and tumor-specific antigens from aberrant cells, activating a targeted immune response. Autologous tumor-based vaccines, which utilize patient-specific TAAs/TSAs, can minimize off-target effects and avoid central tolerance [6–10]. Identifying and including these types of targeted antigens in designing a therapeutic strategy that is precise to specific cancer cells and not expressed in normal cells evades the central tolerance to dodge the off-target effect [11]. Nevertheless, the variable presence of antigens within tumors can lead to immune evasion [12]. Nanoengineering strategies that comprehensively

* Corresponding author. Massachusetts General Hospital, Edwards 211, 50 Blossom Street, Boston, MA, 02114, USA.
E-mail address: htsao@mgh.harvard.edu (H. Tsao).

https://doi.org/10.1016/j.bioactmat.2024.12.023
Received 10 September 2024; Received in revised form 3 December 2024; Accepted 20 December 2024

incorporate the entire spectrum of cellular components, especially membrane proteins, are gaining interest [13–16]. Utilizing these membrane proteins could engage multiple cytotoxic T lymphocyte (CTL) epitopes, thereby enhancing the precision and efficacy of immune targeting [17].

Biomimicry, as realized through nanotechnology [18,19], is an emerging vaccination strategy that can potentially heighten anti-tumor immunity treatment-resistant malignancies like AM and MM. Bio-membranous nanoparticles (BNPs), which are coated with intact cellular membranes, amalgamate the functionality of cell membrane proteins with the cargo capabilities of therapeutic nanoparticles. Source cells for the BNP-based platforms have included red blood cells, tumor cells, immune cells (e.g., macrophages), platelets, and bacteria [20,21]. Despite the promise, BNPs based on monotypic cells are often inadequate to meet the critical intercellular communication for rigorous therapeutic needs [18]. Similarly, cancer vaccination strategies that co-deliver adjuvants and tumor antigens to APCs, such as dendritic cells (DCs), hold great potential compared to other immune treatments [22]. DC vaccine strategies as adoptive cell therapies have highly adaptable activation programs and can stimulate an antigen-specific CTL response controlled by classic MHC-I restricted presentation. However, the short lifespan of the activated DCs and the limited migration of the activated DCs to the draining lymph nodes (LNs) limit the activation of the CTLs. In addition, apposite antigens, immune tolerance, intrinsic DC immunosuppressive factors, and specific delivery mechanisms are some of the major hurdles to clinical utilization [22,23]. The crosstalk between these tumor-derived membrane proteins, DCs, and ultimately CTLs provides an "axis of priming" based on the panoply of epitopes for tumor immunization and establishes a possible strategy for the wholesale transfer of TAAs [24–26].

The inherent ability of DCs to present antigens, manipulate the differentiation of naive $CD4^+$ and $CD8^+$ T cells into T helper/regulatory cells and CTLs, and broadly communicate with other immune cells, make DCs an ideal target for the co-delivery of the TAAs and immunoadjuvants via vaccination [27]. One emerging approach is using hybrid cellular membranes from fused cancer cells and APCs. This fusion cell offers the advantage of providing a continual source of MHC complexes coupled with the entire panoply of tumor antigens [28,29]. Such fusion or hybridization merges the attributes of both individual parent cells, including processing/presentation of whole unidentified and known tumor antigens as well as APC-based immunological co-stimulatory molecules, i.e., B7 family members for enhanced immune responses [30,31].

Vaccines based on whole cell membranes may also enhance tumor targeting through homotypic interactions. Moreover, biocompatibility, biodegradability, and adaptability may be more readily sustainable through this bio-inspired approach. In addition, the membrane proteins of both individual parent cells would have dual targeting capacity to LN and tumor microenvironment (TME) because of homotypic interactions, which can increase payload release and antigen-presentation to T cells in LNs thereby resulting in greater immune activation and tumor inhibition [32]. However, the whole fused-cell-based vaccinations can be carcinogenic, unstable, and difficult to store. A more effective method is to bioengineer cell membrane-based nanovehicles that can preserve critical antigen payloads on the cell surface [33–35] Immunogenicity and cellular and humoral immune responses may also be augmented as these platforms can carry small molecule payloads (e.g., imiquimod, IMQ) that inhibit immune-suppressive mechanisms within the TME [36–38]. Thus, combinatorial nanomedicine using hybrid biomimetic nanoconstructs can be a novel strategy to target treatment-resistant melanomas like those driven by KIT mutagenesis.

2. Results

2.1. Fabrication of a Kit^{K641E}::DC2.4 hybrid cell biomimetic nanovaccine

Overall strategy. We undertook a biomimicry-based nanomedicine approach relying on the membrane proteins of hybrid/fused cells from mutant Kit_{C3}^{K641E} tumor cells and DCs (Fig. 1a). To minimize toxicity, we employed two U.S. FDA (Food and Drug Administration)-approved agents-poly(lactic-co-glycolic) acid (PLGA) as the entrapping polymeric nanovehicle and known TLR7 agonist imiquimod (IMQ, R837) as the drug core of the nanovaccine [39,40]. Because of their biocompatibility, biodegradability, versatility, flexibility, and high loading capacity, PLGA-based NPs have been widely used and proven to be an effective vehicle in the co-delivery and the continuous and controlled release of adjuvants and antigens to APCs and TME, protecting the cargo from premature degradation [41–46]. The mouse model has been previously published [47], and the stages of fabrication are shown broadly in Fig. 1a and detail within the Methods section.

Hybrid fusion cells. Donor membrane proteins were isolated from hybrid Kit_{C3}^{K641E} melanoma/DCs and integrated into PIPNPs to form the full hybrid biomimetic nanovaccines (HBNVs). Polyethylene glycol (PEG) induced amalgamation [48–50] and ethanol treatment to Kit_{C3}^{K641E} to stimulate surface expression of "eat-me" signals [51], and the incorporation of dimethyl sulfoxide (DMSO) finally resulted in the fusion of Kit_{C3}^{K641E} and DCs. To confirm the successful fusion of C3 and DCs, we assessed the expression of CD117/c-kit for Kit_{C3}^{K641E} tumor cells [47,52,53] and CD11c for the DC2.4 cells [54–56]. As shown in Fig. 1b, Kit_{C3}^{K641E} and DC2.4 cells each expressed their cell-specific markers, while $Kit^{K641E}{}_{C3}$::DC fusion cells strongly expressed both CD117 and CD11c.

HBNV construction. It has been reported that NPs between 20 and 200 nm can freely drain into LNs [57], be readily endocytosed by APCs, and successfully stimulate CD4, CD8, and T_h1-type immune responses [58]. Our NPs ranged in mean size from 154 nm to 188 nm with mean polydispersion indices (PDI) of 0.066–0.089, within the target size range with good uniformity (Fig. 1c). As the interstitial fluid comprises mostly negatively-charged proteins, anionic NPs drain more swiftly to LN due to charge repulsion [59,60]. Furthermore, phagocytic cells consume anionic NPs more efficiently than cationic NPs [61]. Since the PNPs were negatively charged (mean zeta potential −22.9 mV), we encapsulated the IPNPs (mean zeta potential −18.6 mV) with a positively charged polyethylene imine (PEI) shell to create PIPNP (mean zeta potential = +11.8 mV). The adhesion of negatively charged Kit_{C3}^{K641E}::DC membrane proteins to the PIPNP led to a reversion of the HBNV charge to a mean zeta potential of −32.2 mV for the HBNV.

These previous [62–65] studies have verified that the PEI-capsuled nanoformulations could effectually adsorb negatively charged antigens, escalate antigen uptake by APCs, augment nanoformulations discharge from the lysosomes, and improve immune responses. Using LC/MS and protein assays, we calculated the mean loading capacities of IMQ and M.P.s in the HBNVs to be 8.87% and 9.79%, respectively. Likewise, the mean entrapment efficiencies of IMQ and membrane proteins in the HBNVs were ~70.98 % and ~78.34 %, respectively (Fig. S1a).

SDS-PAGE demonstrated consistent retention of membrane proteins from the precursor individual cell types to the final HBNV (Fig. S1b). The previous report [66] also showed a similar examination of the ratio of membrane: NP with 0.1, 0.15, 0.2, and 0.3 being the most stable one with better in-range particle size and PDI. In vitro, particle size, PDI, and zeta potentials of the HBNV remained stable for up to 7 days at 4 °C (Fig. S1c). Alexa Fluor 488-conjugated wheat germ agglutinin (WGA), which binds selectively to glycosylated sialic acid residues [25], was also used to validate the proper reconstitution and orientation of the cell membrane proteins in individual single-cell-type biomimetic nanovaccines (Kit_{C3}^{K641E} BNVs, KBNVs; DC2.4 BNVs, DBNVs), and the fused HBNVs (Fig. 1d).

Lastly, the entire structure of the multi-layered HBNV was visually

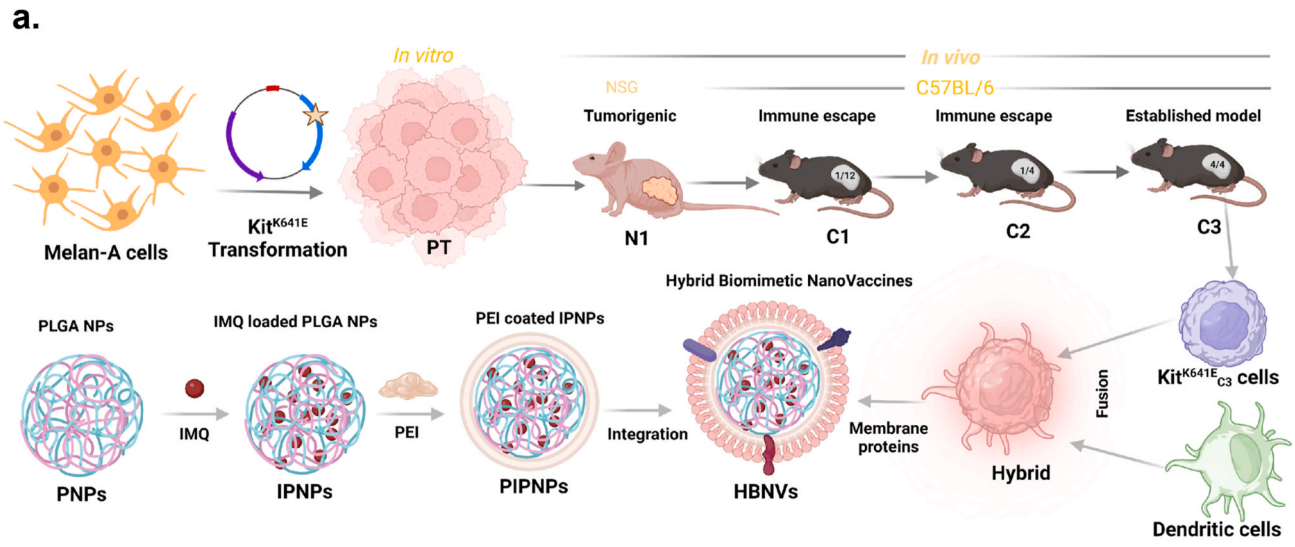

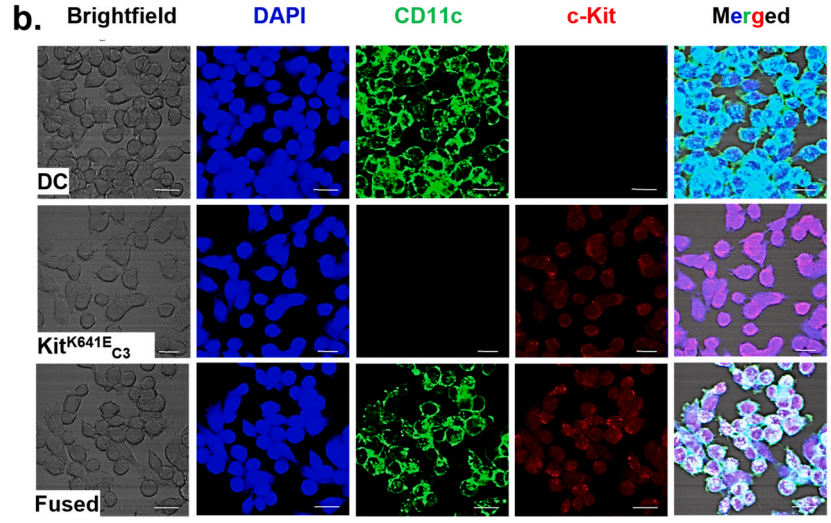

c.

	PNPs	PIPNPs	HBNVs
Mean size (nm)	154.5 (0.7)	167.0 (1.0)	188.7 (18.7)
Mean Z (mv)	-22.9 (2.2)	+12.0 (1.25)	-32.2 (2.0)
Mean PDI	0.089 (0.016)	0.069 (0.014)	0.072 (0.055)

S.D. in parenthesis

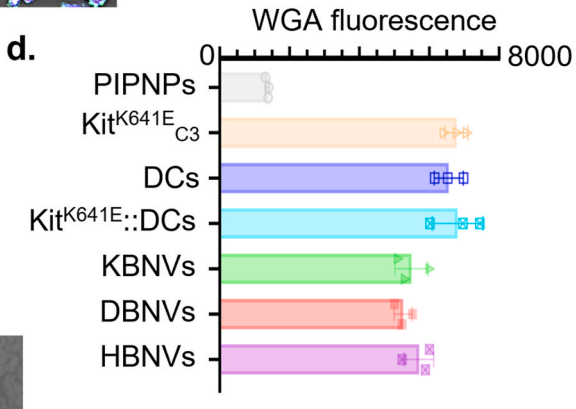

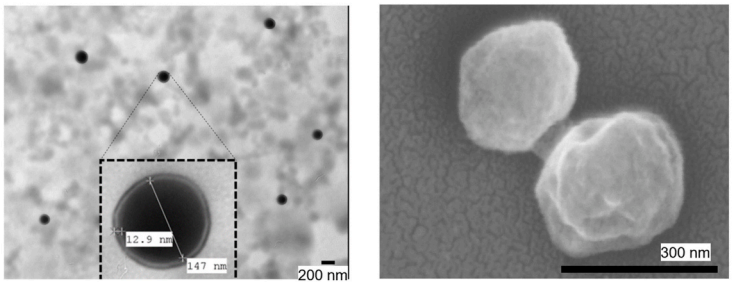

(caption on next page)

Fig. 1. Engineering and characterization of nanovaccine. (a) Cellular derivation for the hybrid biomimetic nanovaccines (HBNVs) based on designations found in Njauw et al. [47]. Briefly, "Pre-tumorigenic" (PT) cells are phenotypically transformed melan-A by cells using *Kit*^{K641E}; these have not experienced any animal hosts. PT cells were then injected into NSG animals, and the first generation NSG tumors ("N1") yielded the "N1" cells. N1 cells were then engrafted into C57BL/6 mice and multiply passaged in C57BL/6 animals (C1, C2, etc) to create the third generation Kit$^{K641E}_{C3}$ cells. Diagrammatic representation of each stage of engineered nanoparticles (NPs); Poly(D, L-lactide-co-glycolide) NPs (PNPs), Imiquimod (IMQ) loaded PNPs (IPNPs), Polyethyleneimine capsuled IPNPs (PIPNPs), and HBNVs from an amalgamation of membrane proteins from fused cells (of Kit$^{K641E}_{C3}$ and dendritic cells (DCs)) and PIPNPs. Scheme was prepared using Biorender.com. **(b)** Confocal laser scanning microscopy (CLSM) examination of fused Kit$^{K641E}_{C3}$ and dendritic cells with overlay of blue fluorescence of 4, 6-diamidino-2-phenylindole (DAPI), red fluorescence of anti-CD117(c-kit)-PE antibody marked Kit$^{K641E}_{C3}$, and green fluorescence of anti-CD11c-FITC antibody labeled DCs, and the merged-labeled fused cells. Scale bar = 20 μm. **(c)** Dynamic light scattering (DLS)-based particle size (nm), zeta potential (Z, mV), and polydispersity index (PDI) analysis of the PNPs and PIPNPs. **(d)** Wheat germ agglutinin (WGA) assay for analysis of glycosylated proteins on the surface of HBNVs. **(e)** Morphological and size characterization of HBNVs by transmission electron microscopy (TEM, scale bar: 200 nm) and scanning electron microscopy (SEM, scale bar: 300 nm). Error bars represent S.D. from three independent experiments; p-values based on Student T-tests with labeled reference (Ref).

observed with TEM, which demonstrated a ~12.9 nm two-layer coat structure encasing an ~147 nm electron-dense IMQ-NP core (Fig. 1e, left panel). SEM demonstrated spherical morphology (Fig. 1e, right panel). These results confirm the intact and expected structure of the HBNV.

2.2. Functional HBNV characterization in vitro and in vivo

HBNVs are selectively internalized by DCs and can promote their functional maturation. Surface proteins on the tumor cell and APCs play critical roles in the successful adhesion and uptake of NPs [13,23,67]. We, therefore, examined the internalization of free sulforhodamine-B (SRB), SRB-loaded PIPNPs, and SRB-loaded HBNVs into DCs and Kit$^{K641E}_{C3}$ cells. As CLSM (Fig. 2a) and flow cytometry (Fig. 2b) demonstrated, DC and Kit$^{K641E}_{C3}$ cells showed significantly higher levels of SRB-HBNV uptake compared to free SRB and SRB-PIPNPs. Furthermore, to determine if membrane identity could direct internalization, we generated distinct SRB-loaded biomimetic NPs from either Kit$^{K641E}_{C3}$ (KBNV) or DCs (DBNV) separately and quantified selective uptake into the two types of cells (Fig. 2c). The capture, processing, and presentation of antigens requires successful drainage and

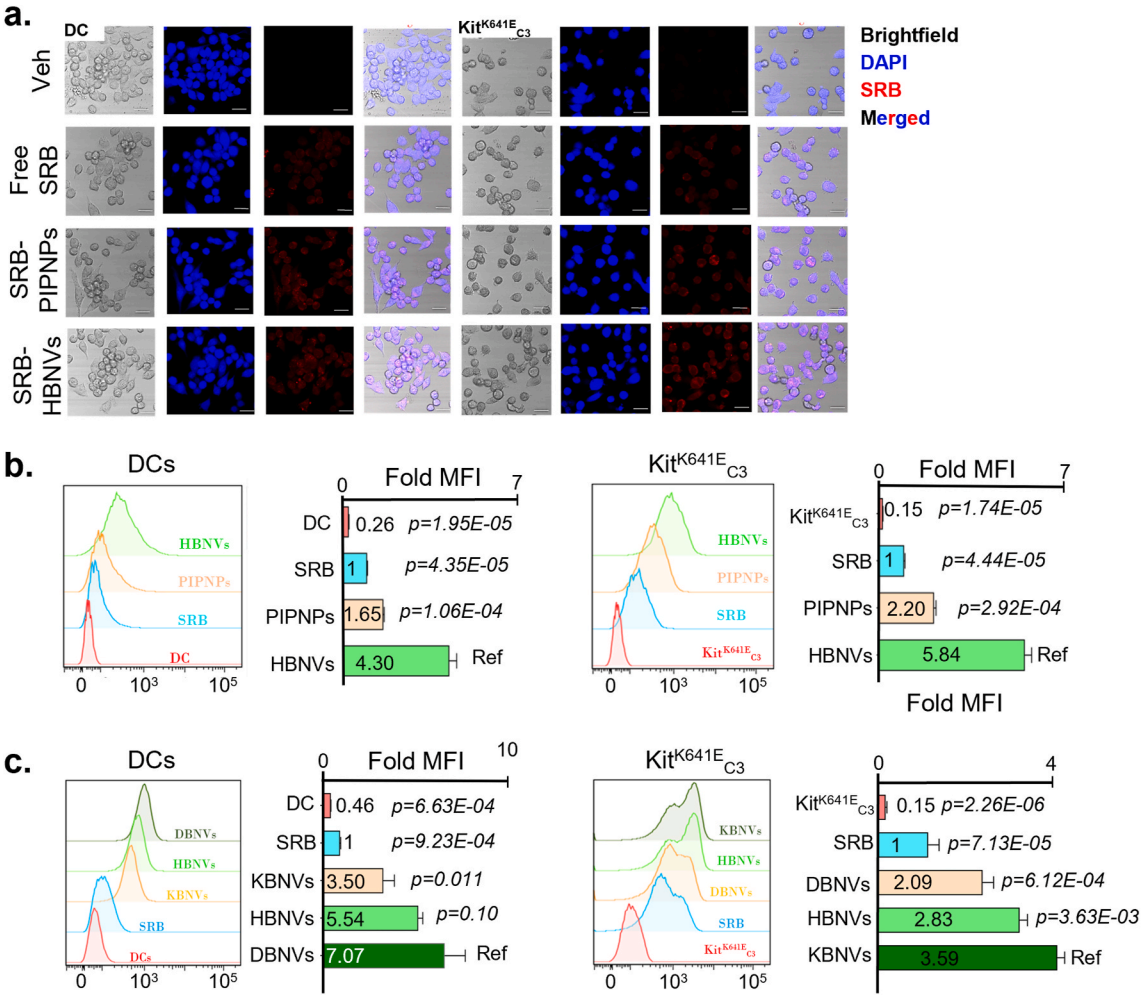

Fig. 2. *In vitro* cellular internalization analysis. (a) Cellular uptake of Sulforhodamine-B (SRB), SRB-loaded PIPNPs, and HBNVs in DCs and Kit$^{K641E}_{C3}$ cells analyzed by confocal laser scanning microscopy (CLSM); nucleus stained by DAPI after 1 h incubation and SRB was loaded as the fluorescent agent. Flow cytometry cellular uptake analysis with comparison of fold (to free SRB) by mean fluorescence intensity (MFI) of **(b)** Uptake of SRB, SRB loaded PIPNPs, and HBNVs in DCs (left two panels) and Kit$^{K641E}_{C3}$ cells (right two panels). **(c)** Uptake of SRB and SRB loaded BNVs created from the membranes of Kit$^{K641E}_{C3}$ cells alone (KBNVs), DC2.4 cells alone (DBNVs), and HBNVs in DCs (left two panels) and Kit$^{K641E}_{C3}$ (right two panels). Error bars represent S.D. from three independent experiments; p-values based on Student T-tests with labeled reference (Ref).

targeting of the nanoformulations to DCs [68]. Normalized to SRB, DCs exhibited a significantly higher uptake of DBNVs compared to KBNVs, while the converse was true for KBNVs and Kit_{C3}^{K641E} cells. The hybrid HBNVs exhibited an intermediate level of internalization into both types of cells.

HBNVs can promote DC function. We next determined if IMQ-loaded HBNVs can function in vitro having documented successful uptake. Markers of APC maturation (CD80 and CD86) were first assessed by exposing cultured DCs to IMQ, the various NPs, and LPS as a positive control. HBNV treatment led to the highest mean percentage of $CD11c^+CD80^+CD86^+$ cells (Fig. 3a). Free IMQ and PIPNPs led to a strong induction of $CD11c^+CD80^+$ cells but very little $CD11c^+/CD86^+$ DCs (Figs. S2a–b).

Secreted cytokines after the treatment of the formulations are crucial signs of DC maturation and immunomodulation [69]. Tumor necrosis factor-alpha (TNF-α) secretion was analyzed owing to its potential to induce the expression of co-stimulatory molecules and MHC molecules on the surface of DCs, enabling maturation and activation, migration and homing of DCs to lymphoid organs, stimulation of immune-activating cytokines (IL-12, IL-6) production, and cross-presentation [70,71]. Likewise, interleukin-12p40 (IL-12p40) is also responsible for the enhanced antigen presentation and promotion of Th1 responses, stimulating the production of interferon-gamma (IFN-γ) by T cells and natural killer (NK) cells [72]. By ELISA, HBNV treatment significantly increased the release of pro-inflammatory cytokines (Fig. 3b) TNF-α, IL-12p40, and IL-6; both IMQ and PIPNPs also stimulated the release of albeit to a lesser extent. For IL-10 (Fig. 3c), both free IMQ and PIPNPs significantly increased IL-10 secretion; however, HBNVs partially abrogated this effect, dramatically reducing IL-10 levels compared to IMQ or PIPNPs.

T-cell activation against tumors critically depends on the antigens and immunostimulants taken up to activate and mature DCs [73]. TLR

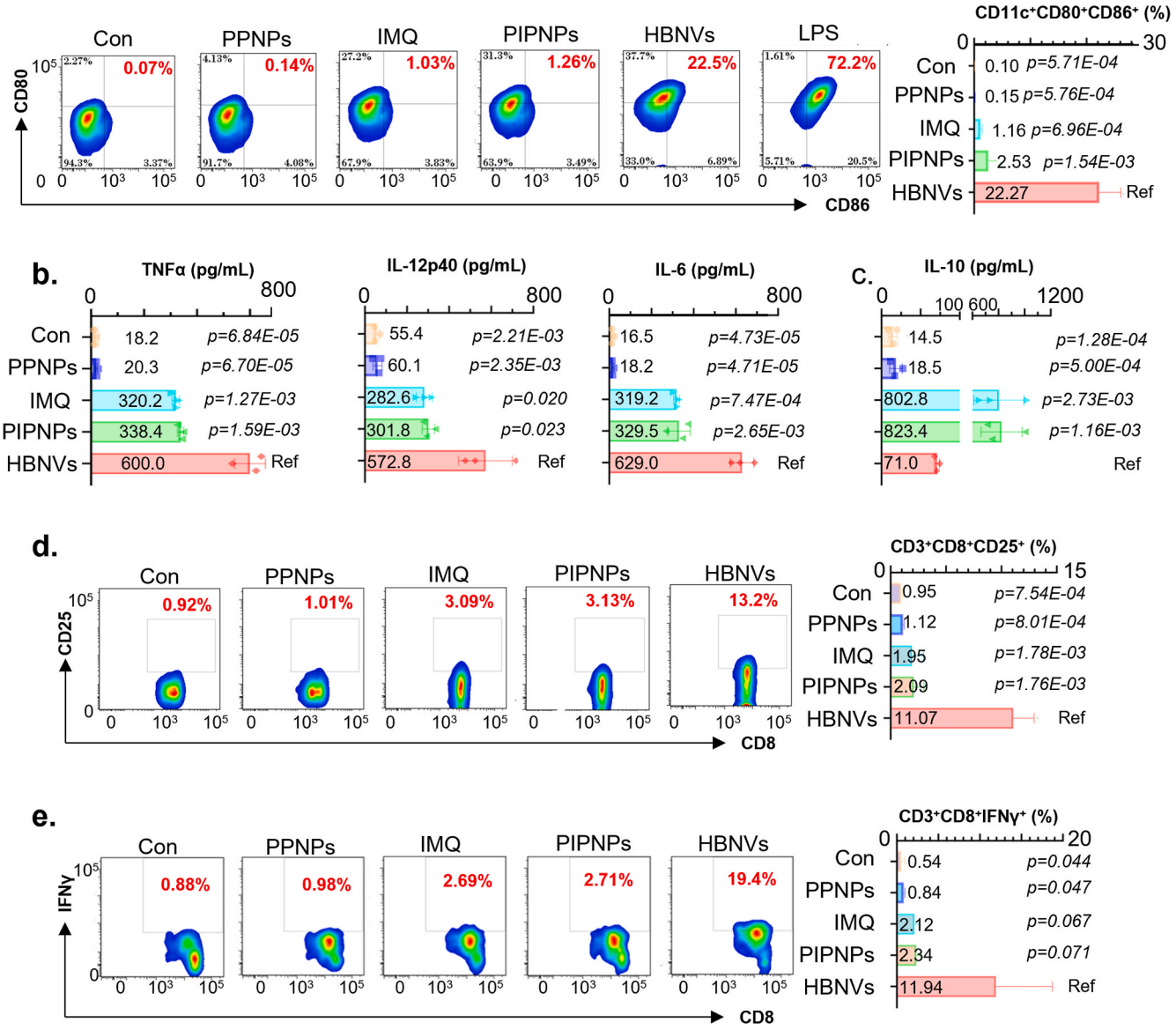

Fig. 3. ***In vitro*** **maturation, cytokine release, and T cell activation analysis. (a)** Flow cytometric quantitation of mature DCs ($CD11c^+CD86^+CD86^+$) after treatment with control vehicle (Con), PPNPs, IMQ, PIPNPs, and HBNVs for 48 h. ELISA analyses of secreted **(b)** immunostimulatory cytokines (TNF-α, IL-12p40, and IL-6) and **(c)** immunosuppressive IL-10 by DCs after treatment with Con, PPNPs, IMQ, PIPNPs, or HBNVs to DCs. **(d)** *In vitro* T cell activation assay. DCs were treated with Con, PPNPs, IMQ, PIPNPs, or HBNVs and co-cultured with $CD8^+$ T cells. Flow cytometric determination of T cell activation with the evaluation of $CD3^+CD8^+CD25^+$ T cells after the co-culturing with the treated DCs. **(e)** Analysis of IFN-γ-producing $CD8^+$ T cells after co-culture with DCs treated with vehicle, PPNPs, IMQ, PIPNPs, and HBNVs. Error bars represent S.D. from three independent experiments; p-values based on Student T-tests with labeled reference (Ref).

agonist IMQ and antigenic proteins mediated DC maturation were anticipated to be significantly helpful in generating all necessary signals for the activation of T cells. Using a co-culture system, we first treated DCs to the various formulations and then subsequently exposed splenic-derived lymphocytes to the pre-treated DCs. DCs pre-treated with the HBNV induced a significantly higher percentage of $CD8^+CD25^+$ (Fig. 3d) and a trend towards higher $CD3^+CD8^+IFN\gamma^+$ cells (Fig. 3e) than naked PIPNPs. Taken together, these results indicate that HBNVs are internalized to a greater extent than their naked NP counterparts, possibly through selective homotypic interactions, and that the HBNVs can successfully induce DC maturation and mediate subsequent $CD8^+$ T cell stimulation and activation in vitro.

HBNVs home to LNs and can activate DCs. Biodistribution of the HBNVs can potentially influence their ability to successfully engage and stimulate the immune system. Thus, we analyzed the homing of the HBNV to draining inguinal lymph nodes (iLNs) and to off-target vital organs. Free SRB and SRB-loaded PIPNPs and HBNVs were separately injected into the subcutaneous compartment at the tail base of mice [25,48,74], followed by IVIS imaging of dissected ex vivo organs 24 h after administration. Fig. 4a shows representative ex vivo organs, while Fig. 4b shows the mean fluorescent signals in those organs. Free SRB was taken up mainly in the liver, while SRB-loaded PPNPs were primarily localized to the liver and spleen (Fig. 4b*)*. However, SRB-loaded HBNVs trended towards greater accumulation in ins compared to SRB (3.68-fold, p = 0.085) and SRB-PPNPs (4.86-fold, p = 0.068). The off-target effect of the SRB-HBNVs on the liver was lower than SRB-PPNPs (Fig. 4b), making the HBNVs potentially more biocompatible. In vivo stability analysis using SRB-loaded HBNVs showed continued and selective accumulation of the HBNV in iLNs compared to free SRB at 48 h and 72 h after administration, though there was some diminution possibly due to fluorescence clearance and quenching (Fig. S3). Taken together, the presence of membrane proteins from DCs and $Kit^{K641E}{}_{C3}$ cells, such as MHC, adhesion, and co-stimulatory molecules, likely promotes the targeting of the nanovaccine into draining LNs while minimizing off-target effects [48].

Given the evidence of nodal homing, the amount of cellular uptake of free SRB, SRB-PIPNP, and SRB-HBNVs by iLN cells was then evaluated (Fig. 4c). Dissected iLNs were digested, and the dissociated cells were subjected to flow cytometry. iLN cells from animals injected with SRB-HBNVs exhibited much higher fluorescent levels than those injected with either SRB-PIPNPs or free SRB. Bio-TEM also verified the intracellular accumulation of abundant ~150–200 nm NPs within both iLN and tumor cells by subcutaneous injection (Figs. S4a and b) or intratumoral injection (Fig. 4c).

To more specifically quantify HBNV internalization by DCs, iLN cells were subjected to flow cytometry with anti-CD11c. Injection of SRB-HBNVs led to a significantly higher percentage of SRB+/CD11c + cells in the iLNs than SRB-PIPNPs (Fig. 4d; 3 animals each). In vivo DC maturation was also investigated by injecting free IMQ and the various nanoconstructs into mice (n = 3 mice for each condition). iLNs were dissected, dissociated, and subjected to flow cytometry using anti-CD11c, anti-CD80, and anti-CD86 (Fig. 4e). HBNV treatment led to the highest percentages of $CD11c^+CD80^+CD86^+$ cells, followed by IMQ and PIPNP. These data indicate that HBNVs can selectively home to iLN and synergistically induce significantly greater DC maturation compared to free IMQ and IMQ-incorporated PIPNPs. We also examined evidence of immune stimulation by the HBNV in the draining iLN. As shown in Fig. S5, CLSM showed an increased flux of $CD8^+$ cells in the iLN after SC vaccination with the HBNV compared to controls.

HBNVs demonstrate tumor homing in vivo. While we have shown the homing of iLNs by HBNVs, it is unknown whether membrane identity can confer selective tumor targeting in the animal. To assess HBNV tumor targeting, we compared the uptake of subcutaneously injected SRB-PIPNPs, SRB-DBNVs, SRB-KBNVs, and SRB-HBNVs in the Kit^{K641E}_{C3} tumors. As shown in Fig. 4f and g, there was significantly more tumoral uptake of SRB-KBNVs than SRB-DBNVs; SRB-HBNVs exhibited more than SRB-DBNVs but not significantly. DBNVs and KBNVs predominantly homed to iLNs and tumors, respectively, while HBNVs showed an intermediate balance between the two compartments (Fig. 4h). These results show that HBNVs preferentially migrate and accumulate in both the tumor and iLNs, potentially making HBNVs an effective delivery vehicle into the two compartments necessary for immune activation (e.g., priming phase) and tumor destruction (e.g., effector phase).

2.3. In vivo assessment of HBNV efficacy

Therapeutic vaccination with HBNVs reduces tumor progression (Trial 1, T1). We first analyzed the efficacy of HBNV as a therapeutic vaccine (protocol, Fig. 5a). C57BL/6 mice were injected with Kit^{K641E}_{C3} cells on day −14 and were treated with either vehicle or free IMQ, or immunized with PPNPs, PIPNPs, or HBNVs on days −4, 0, and +4.

As shown in Fig. 5b, The HBNV, PIPNP, and free IMQ arms led to 76.0 % (p = 4.95E-16), 26.9 % (p = 4.39E-06) and 31.0 % (p = 1.38E-04) reductions in mean tumor volume (TV), respectively, relative to control vehicle. HBNV treatment was significantly better than either free IMQ (p = 6.08E-08) or PIPNP (p = 2.15E-08) alone. Tumor growth was indistinguishable between the control vehicle and PPNP (p = 0.97) and between IMQ and PIPNP (p = 0.56). There was no significant difference in the mean TV between male and female mice (267.3 mm^3 vs 257.5 mm^3, p = 0.83).

Confocal laser scanning microscopy of tumor specimens (Fig. 5d and e) showed that HBNV-treated mice exhibited a significantly greater infiltration of intratumoral $CD8^+$ T cells compared to tumors from the animals exposed to vehicle control, PPNPs, free IMQ, and PIPNPs. Both IMQ and PIPNP treatments were also associated with a significantly higher percentage of $CD8^+$ T cells compared to vehicle control and PPNPs. Flow cytometry of dissociated tumor cells also showed that the HBNV-treated tumors have the highest mean percentage of $CD3^+CD8^+$ cells (Fig. 5f and g).

Regulatory T cells (Treg) cells can suppress DC function, effector T cells, modulate the cytokine milieu, maintain peripheral immune tolerance, and promote angiogenesis to tumor growth [75]; therefore, balanced CTL/Treg activity is critical for effective tumor inhibition without causing autoimmune pathology [76]. As such, we next quantified intratumoral levels of $CD4^+FoxP3^+$ T cells by flow cytometry (Fig. 5h and i). HBNV-treated tumors harbored a significantly lower percentage of$CD4^+FoxP3^+$ cells than free IMQ and PIPNP-treated tumors and the highest ratio of CD8:Treg cells (Fig. 5i).

Lastly, macrophage polarization is also known to influence tumor cell killing with the M1 phenotype associated with pro-inflammatory (i.e., anti-tumor) responses and the M2 phenotype linked to anti-inflammatory (i.e., pro-tumor) properties [77]. Dissociated intratumoral macrophages ($CD11b^+F4/80^+$ cells) were measured by flow cytometry and stratified into M1 and M2 subgroups using anti-CD80 and anti-CD206 antibodies, respectively (Fig. 5j and k). While there were no significant changes in the intratumoral levels of $CD80^+$ cells, there was a significant decrease in the mean percentage of $CD206^+$ macrophages (control = 7.87 % vs. HBNV = 3.31 %, p = 0.023), leading to a significant increase in the mean M1/M2 ratio (HBNV = 5.35 vs. control = 1.50, p = 0.046). Taken together, HBNVs appear to induce CD8 T cells, reduce Tregs, and polarize macrophages towards an M1 phenotype, all of which support the observed strong clinical efficacy.

Primary immunization with HBNV prevents tumor onset (Trial 2; T2). Prophylactic vaccination against cancer has been used mostly on viral-induced tumors such as HPV and HCV [78]. While primary vaccination has not been fully explored in non-viral human malignancies, we set out to test the effectiveness of HBNV as a prophylactic vaccine. Animals were treated with two rounds of free IMQ or immunized twice with PPNPs, PIPNPs, or HBNVs (days −28 and −21). $Kit^{K641E}{}_{C3}$ cells were then injected into the subcutaneous tissue on Day −14, with tumor measurements starting at Day 0 (Fig. S6a). Unlike the

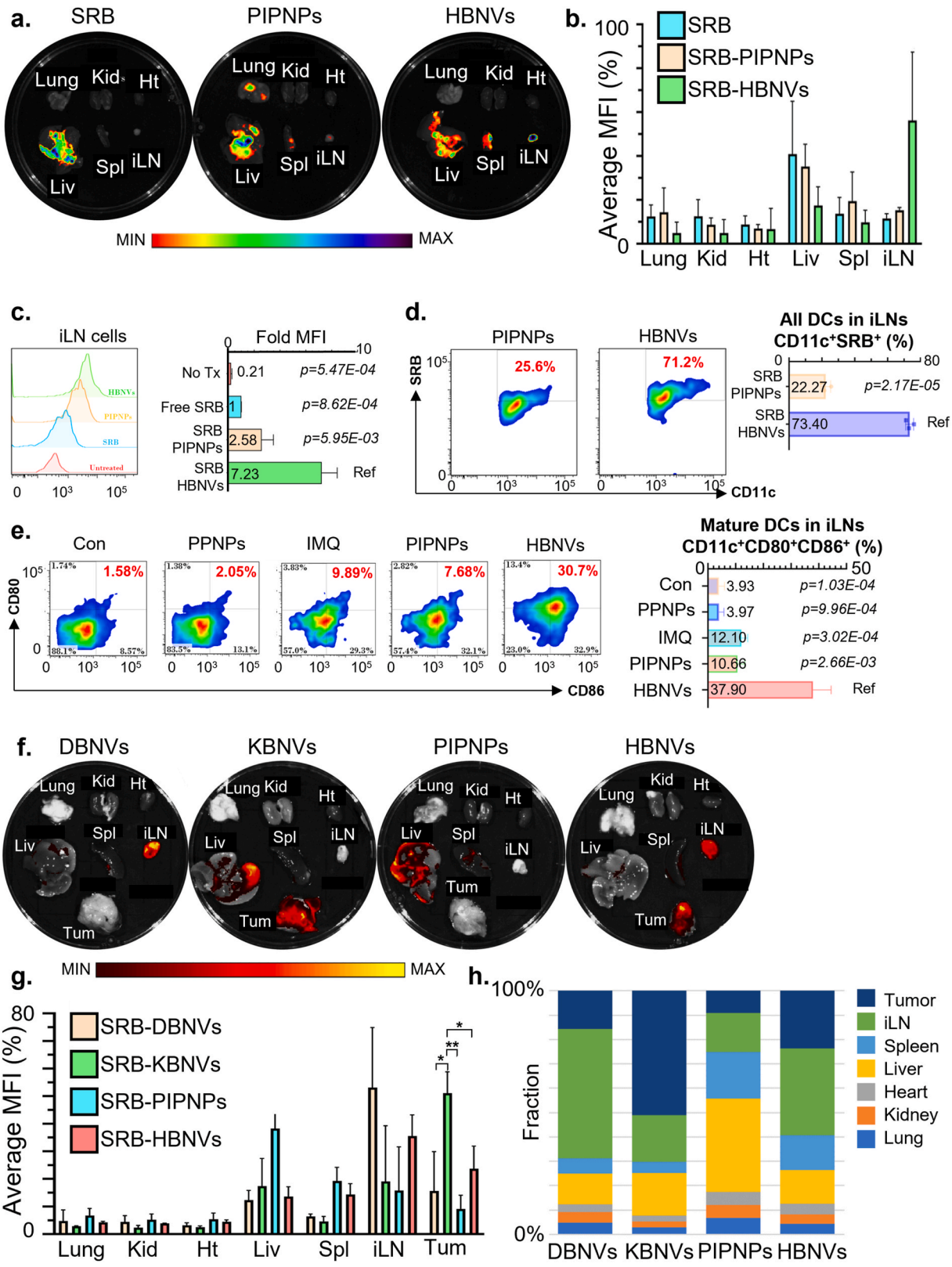

Fig. 4. Biodistribution and DC targeting/maturation analysis. Quantitative comparative imaging (IVIS Spectrum) of ex vivo organs 24 h after subcutaneous administration of SRB, SRB-loaded PIPNPs, and HBNVs into the tail base of C57BL/6 mice. **(a)** Images and **(b)** quantitation of SRB mean fluorescence intensity (MFI) of lungs, kidneys (Kid), heart (Ht), liver (Liv), spleen (Spl), and inguinal lymph nodes (iLNs) in tumor naive mice. **(c)** Flow cytometric quantification of SRB MFI in **(c)** dissociated iLN cells and **(d)** CD11c + DCs in iLN. **(e)** Flow cytometric quantitation of mature iLN DCs ($CD11c^{+}CD80^{+}CD86^{+}$) after the administration of vehicle, PPNPs, IMQ, PIPNPs, and HBNVs. **(f)** Ex vivo images (of lungs, kidneys, heart, liver, spleens, iLNs, and tumors in tumor inoculated mice, and **(g–h)** comparative SRB quantitation after subcutaneous administration of SRB, SRB-loaded PIPNPs, and HBNVs into the tail base of C57BL/6 mice after 24 h.

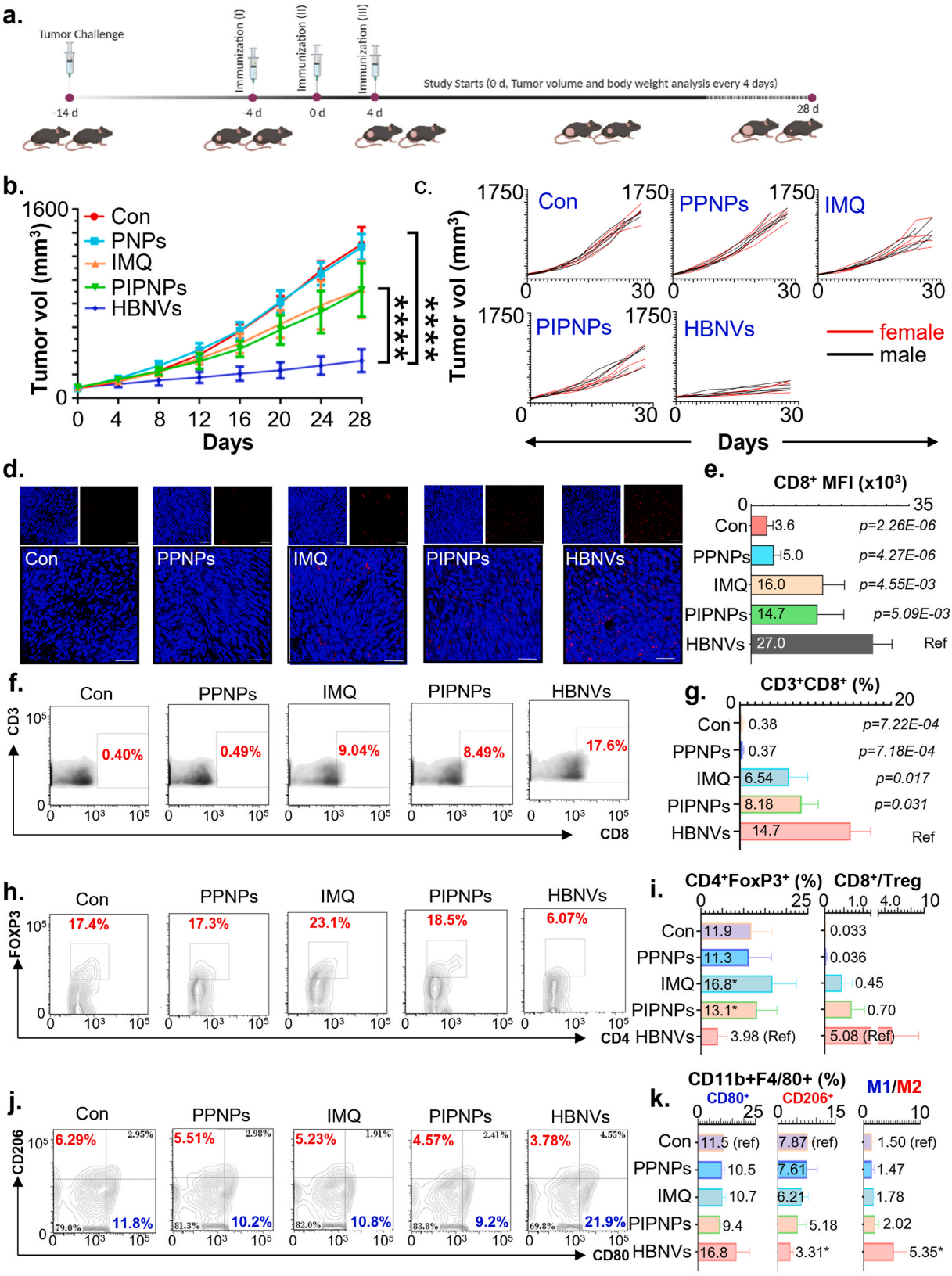

Fig. 5. Therapeutic efficacy of HBNVs. (a) Experimental scheme showing the immunization, tumor challenge, and study details. Time-course analysis of **b**) tumor growth (n = 6 mice, 3 male and 3 female, up to day 28), **c)** spider curves (n = 10 mice, 5 male and 5 female, n = 10, up to day 28). **(d)** CLSM imaging (scale bar = 50 μm) and **(e)** quantitation of intratumoral $CD8^+$ T cells after treatment with Control, PPNPs, IMQ, PIPNPs, and HBNVs. **(f–g)** Flow cytometric and quantitative analyses/comparison of intra-tumoral $CD8^+$ T cells ($CD3^+CD8^+$) after cell dissociation. Flow cytometric analyses of intratumoral regulatory T cells (Tregs, $CD3^+CD4^+FoxP3^+$) and $CD8^+$/Treg ratio **(h–i).** Phentotype of intratumoral macrophages, M1 ($CD11b^+F4/80^+CD80^+$), M2 ($CD11b^+F4/80^+CD206^+$), and M1/M2 ratio **(j–k).** ****$p < 0.0001$.

therapeutic trial, animals treated with PPNPs, free IMQ, and PIPNPs did not exhibit any clinical benefit above control animals (Figs. S6b–c). However, animals primarily vaccinated with the HBNV showed a significant suppression of tumor growth (HBNV, mean TV = 274.8 mm^3 vs control mean TV = 992.3 mm^3, p = 2.43E-08). As with Trial 1, there was no difference in mean TV between male and female mice.

Animal toxicity. No notable adverse events were found in either trial. There were no differences in body weight between any treatment groups apart from the changes in body weight from the tumor burden (Figs. S7a–b). Furthermore, organ toxicity (heart, liver, lungs, kidneys, spleen, and iLNs) due to the HBNVs was examined and compared to the vehicle group using histopathological analysis (Fig. S7c), and no visible differences were found.

2.4. Molecular characterization of tumors

Differentially expressed genes (DEG) and pathway analyses of tumors. To broadly delineate HBNV-associated molecular changes in the tumors, we performed bulk RNAseq on control and HBNV-treated tumors from both the prophylactic and therapeutic trials (Tables S1–S2). Principal component analysis (PCA) of all tumors showed a tight clustering of T1 and T2 control samples within the expression space. However, there were no distinct patterns for HBNV-treated tumors between T1 and T2 (Fig. 6a). Volcano plots for T1 and T2 revealed much more significant changes with T1 compared to T2 (Fig. 6b).

Trial 1 tumors. Between control and HBNV-treated tumors (Fig. 6b, left panel; Table S3), 8300 genes exhibited a significant difference in expression ($P_{adj} < 0.05$). Among these, 4315 (52 %) genes and 1184 (14 %) genes were upregulated ($FC_{log2} > 1$) and downregulated ($FC_{log2} < -1$) by greater than 2-fold, respectively.

Gene ontology (GO) interrogation of DEGs between control and HBNV-treated tumors using over-representation analysis (ORA) found that the top 5 upregulated biological process (BP) terms all involved immune stimulation (Fig. 6c; left panel; Table S4). These included the production of molecular mediator of immune response (FDR = 2.69E-63), immunoglobulin production (FDR = 2.02E-53), immune response regulating signaling pathway (FDR = 1.17E-52), positive regulation of leukocyte activation (FDR = 2.20E-47), and positive regulation of cell activation (FDR = 1.95E-46). The top downregulated GO-BP terms were functionally enriched for TGFβ signaling and ECM: cellular response to TGFβ stimulus (FDR = 2.46E-12), response to TGFβ (FDR = 3.61E-12), TGFβ receptor signaling pathway(FDR = 2.70E-11), ossification (FDR = 1.37E-10), and extracellular matrix organization (FDR = 1.37E-10) (Fig. 6c; right panel; Table S4). KEGG interrogation of tumors identified TH17 cell differentiation (FDR = 7.07E-13) as the top upregulated pathway in addition to B cell receptor signaling (FDR = 2.31E-11) and TH1/TH2 cell differentiation (FDR = 2.31E-11) (Fig. 6d, left panel; Table S4). Top downregulated KEGG pathways (Fig. 6d, right panel) included focal adhesion (FDR = 4.31E-13), protein processing in endoplasmic reticulum (FDR = 2.33E-08), and hippo signaling pathway (FDR = 3.99E-08). CNET plots (Fig. 6e and f) revealed several critical relationships between gene sets and GO-BP enriched terms. Notably, genes involved in immunoglobulin production and TGFβ were significantly upregulated and downregulated, respectively.

Fig. 6g and h show the top gene set enrichment analysis (GSEA) upregulated (orange) and downregulated (blue) gene sets for GO-BP and KEGG, respectively (Table S4). Again, multiple gene sets related to immune activation were positively enriched (e.g., adaptive immune response, NES = 2.02, FDR<2.2E-16; allograft rejection, NES = 1.94, FDR<2.2E-16); once again, response to TGF-β was negatively enriched (NES = −1.85, FDR = 0.0063) along with Hippo signaling gene sets.

Trial 2 tumors. For the prophylactic trial (T2) tumors, PCA (Fig. 6a) showed a similar dispersion of the HBNV tumors, overlapping with the T1 HBNV tumors. However, unlike the T1 tumors, there were only 3852 DEGs ($P_{adj} < 0.05$) with 2591 (31 %) upregulated and 371 (4 %) downregulated genes with HBNV treatment (Fig. 6b, right panel; Table S5). Gene expression profiles from the six HBNV therapeutically treated and six HBNV prophylactically treated tumors showed an extremely tight correlation (Fig. S9; $R^2 = 0.99$; $p < 0.0001$). Among the top 50 most upregulated GO-BP terms, 45 were shared between T1 and T2 tumors. Similarly, 38 of the top 50 most upregulated KEGG pathways overlapped between T1 and T2 tumors (Tables S6–S7). These results suggest that the fundamental molecular response to the HBNV is similar in both the prophylactic and therapeutic settings.

Immune cell profiling. Next, we deconvoluted the bulk RNAseq data into immune cell profiles. Since T1 and T2 tumors showed similar pathways and expression profiles, we combined the RNAseq analysis into two groups-all untreated controls and all HBNV-treated tumors. xCell (Fig. 7a), Quantiseq (Fig. S9a), and MMPC Counter profiles (Fig. S9b) all consistently identified B cells and $CD8^+$ T cells as significantly upregulated by HBNV (Table S8). In addition, xCell estimations also revealed significant increases in aggregate immune ($p < 0.000001$) and TME ($p < 0.000001$); notably, there was also a substantial decrease in the CAF score ($p < 0.000001$).

To examine coordinated immune responses, we used the xCell scores available for 39 immune cell types in all 24 treated and untreated tumors to perform hierarchical clustering (Fig. 7b; Table S9). Three classes of tumors emerged. Class 1 (C1) tumors exhibited high B cell/$CD8^+$ T cell transcripts, while C2 tumors harbored higher monocyte/macrophage transcripts with much sparser B cell/$CD8^+$ T cell signatures. Class 3, which includes all the control untreated tumors, consistently showed a strong CAF signature but little or no inflammation. In terms of mean tumor volumes, both C1 (mean TV = 234.2 mm^3) and C2 (MTV = 234.2 mm^3) samples were significantly smaller than C3 tumors (MTV = 863.6 mm^3; C1 vs C3, p = 0.0005; C2 vs C3, p = 0.0013) (Fig. 7c). Interestingly, 3 of 12 HBNV-treated tumors (all male T1 tumors, Fig. 7c, green circles) fell into C3, though its tumor volumes were comparable to C1 and C2 tumors. While the mechanism is unknown, these HBNV-treated C3 tumors may reflect a temporal issue whereby there is a downregulation of immune infiltration after the initial HBNV-mediated tumor response or immune cell exhaustion or a sampling issue whereby tumor inflammation was underrepresented in the RNA-sequenced zone. As mutation-derived neo-epitopes on the HBNV membranes could incite inflammation, we also examined the mean tumor mutation burden (MTMB) among the three classes (Fig. 7d). Strikingly, C3 tumors had significantly higher MTMB (n = 700.9) compared to C1 (n = 626, p = 6.12E-09) or C2 (n = 589.5, p = 2.10E-05) tumors, thus providing supportive evidence for in vivo immunoediting. The relationship between TV and TMB exhibited a threshold effect with a cutoff at TMB ñ675 (Fig. 7d, dotted line).

The robust stimulation of B cells observed with HBNV vaccination suggests that tertiary lymphoid structures (TLS) may be generated with the treatment. As most of the tumor was used for RNA analysis, we did not observe definitive evidence of TLS in the available pathological sections. Nevertheless, several TLS gene signatures have been described [79–83] and can thus be used for molecular TLS detection (Fig. S10; Table S10). A 29-gene TLS imprint signature [83] derived from human renal cell carcinoma showed significantly higher median levels of aggregate expression in HBNV-treated animals compared to control animals (median aggregate RNA expression HBNV vs control: 58.0 vs. 715.5, Mann Whitney $p < 0.0001$). Similarly, increased TLS gene expression levels were also identified for an 18-gene Th1/B cell TLS signature derived from human gastric cancer [84] median aggregate HBNV expression vs. control expression: 98.0 vs 626.0, Mann Whitney $p < 0.0001$) and a 9-gene TLS signature from human melanomas [82] (median aggregate HBNV expression vs. control expression: 43.5 vs 72.0, Mann Whitney p = 0.0028).

We also looked at differences in the immune response to the HBNV based on sex. Compared to males, females exhibited a more robust immune response overall (Fig. 7e). xCell analysis of the HBNV-treated tumors showed that females had significantly higher mean xCell

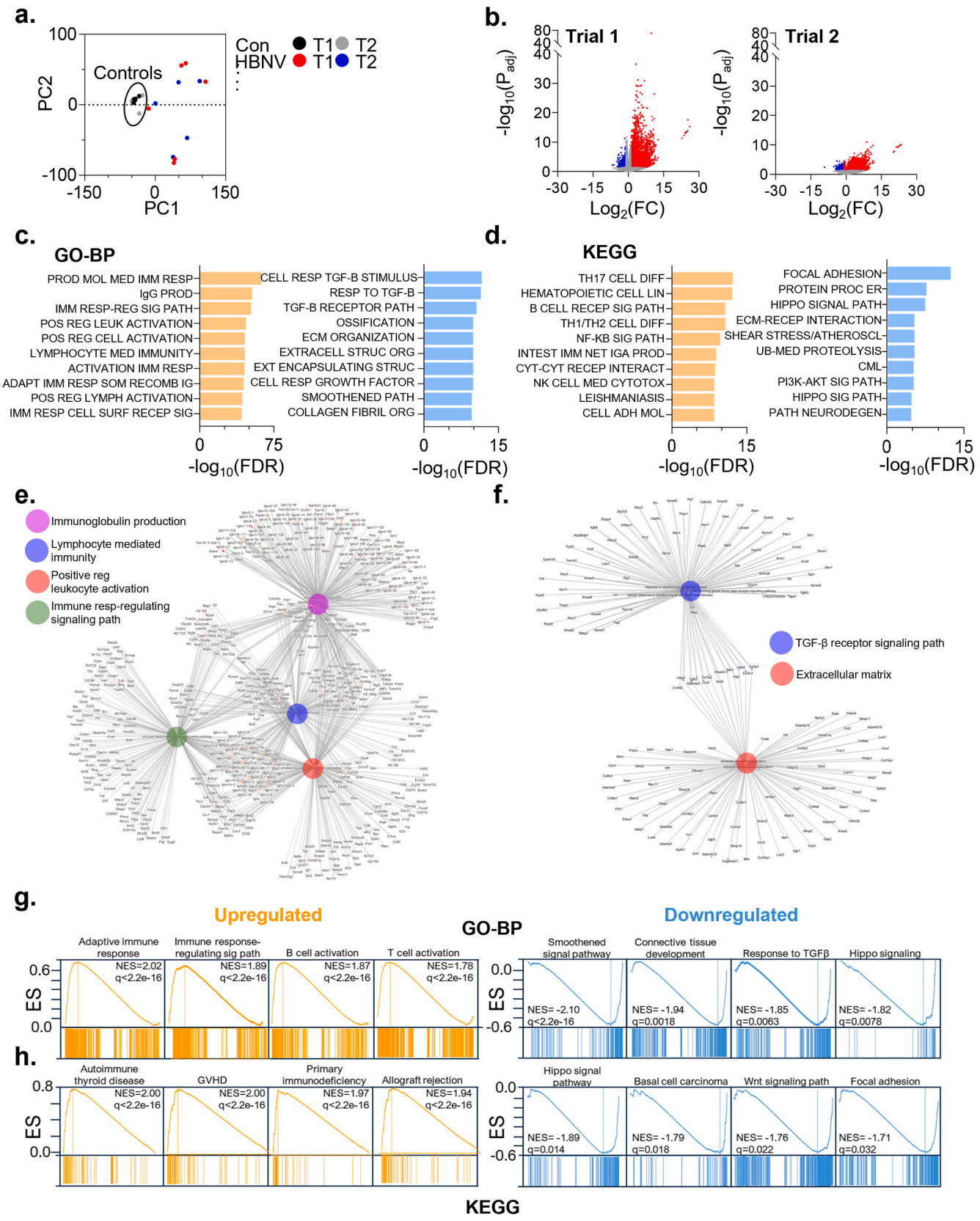

Fig. 6. Molecular analysis of HBNV tumors. (a) Principal component analysis of tumors from vehicle-treated control animals (T1 therapeutic trial, black circles, n = 3 males/3 females; T2 prophylactic trial, grey circles, n = 3 males/3 females) and HBNV treated animals (T1, red circles, n = 3 males/3 females; T2 blue circles, n = 3 males/3 females). **(b)** Volcano plot of differentially expressed genes (DEGs, red dots: fold change>2 upregulated HBNV vs Con, $P_{adj} < 0.05$; blue dots: fold change>2 downregulated HBNV vs Con, $P_{adj} < 0.05$) using DESeq2. **(c)** Top gene ontology biological process (GO-BP) and **(d)** KEGG pathways from functional analyses of DEGs (orange bars, upregulated; blue bars, downregulated) using ClusterProfiler. Cnet plots for **(e)** upregulated and **(f)** downregulated gene IDs and nodes.

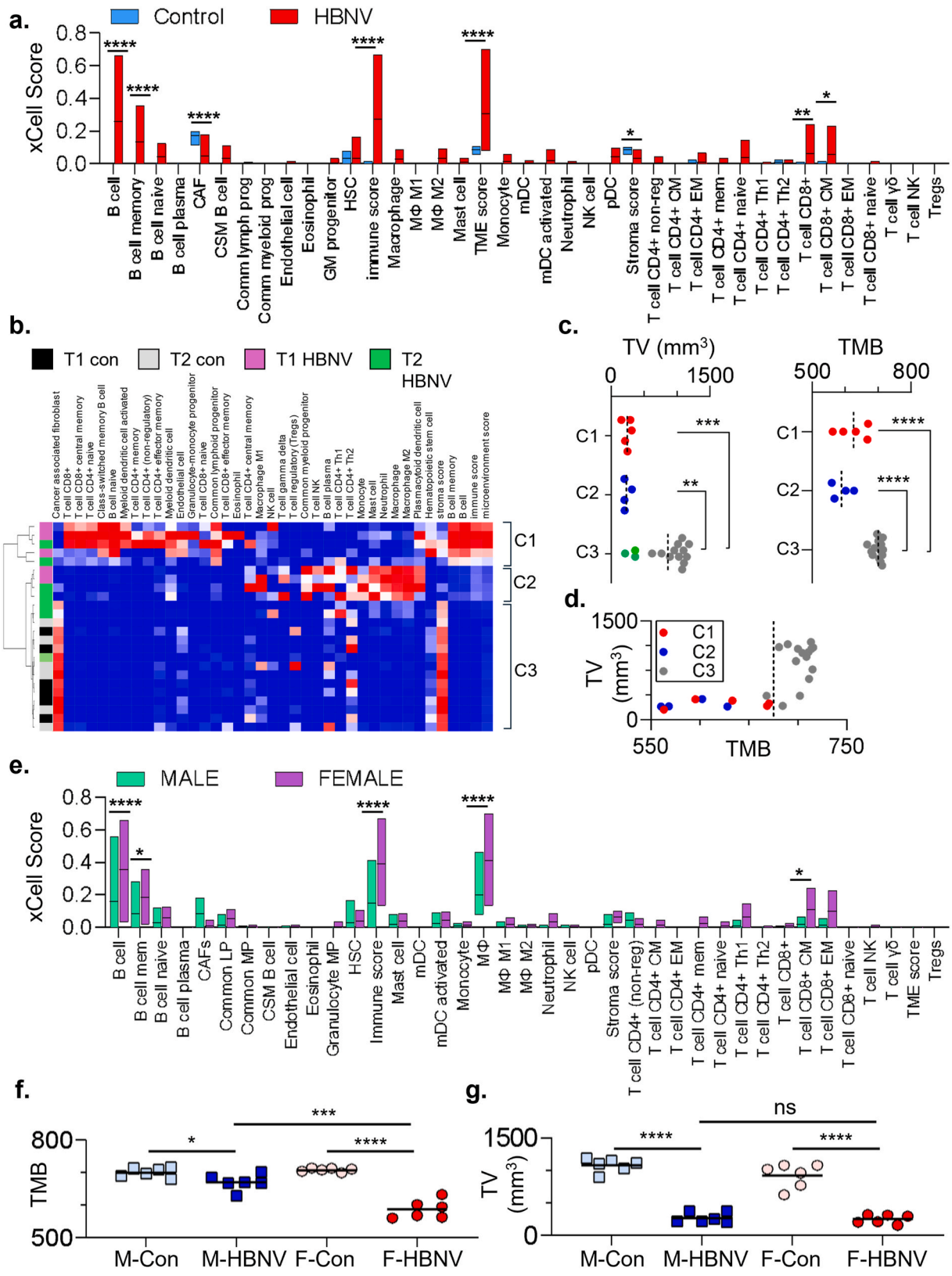

Fig. 7. Immune profiling of tumor. **(a)** Mean xCell scores for various immune cell subsets by treatment exposure. **(b)** Multidimensional hierarchical clustering using xCell scores and immune cell class. Performed with Morpheus (https://software.broadinstitute.org/morpheus/) using Euclidean distance and complete linkage. **(c)** Tumor volume (TV in mm^3) and tumor mutation burden (TMB counts) for Class 1 (C1, red circle), Class 2 (C2, blue circles) and Class 3 (C3, high volume tumor: grey circles, low volume tumors: green circle). **(d)** Plot of TV vs TMB. **(e)** Mean xCell scores for the various immune cell classes by sex. Comparison of TMB **(f)** and TV **(g)** between various sex and treatment groups (M, male, F, female). *$p < 0.05$, **$p < 0.01$, ***$p < 0.001$. ****$p < 0.0001$.

scores for memory B cells, B cells, $CD8^+$ T central memory cells, immune score, macrophage, and TME score. As TMB has also been shown to be higher in melanomas in men compared to women [85], we assessed the TMB in these tumors (Fig. 7f). There was no significant difference in the MTMB between the 6 male and 6 female control mice. However, HBNV treatment significantly reduced MTMB for both male and female tumors ($P_{male} = 0.02$ and $P_{female}<0.0001$). Also, compared to HBNV-treated male tumors, female HBNV-treated tumors had significantly fewer mutations ($p = 0.0003$). Regarding TV (Fig. 7g), there were significant changes with HBNV treatment in both male and female mice compared to control, though sex was not a significant factor ($p = 0.64$). Together, these immune profiles confirm that inflammation (e.g., Class 1 and 2) is a fundamental corollary of tumor response and that biological sex may play a role in mutation pruning of the tumors.

3. Discussion

Rare, treatment-resistant cancers remain a critical unmet need in the landscape of cancer therapeutics. Acral lentiginous and mucosal melanomas (ALMMs) are emblematic of this challenge. These subgroups have genetic and molecular characteristics different from the more common forms of melanoma. For example, ALMMs have lower tumor mutation burdens [1–4] and are more likely to carry KIT mutations. These differences likely contribute to the low response rates to both immune and molecular treatments designed for non-acral metastatic melanomas [1–5]. For ALMMs, clinical responses to molecular and immune therapies have been underwhelming compared to the successes reported for other types of melanoma. A meta-analysis of c-Kit inhibitors in 601 patients across 19 melanoma trials revealed an aggregate overall response rate (ORR) of only 13 % [86]. Similarly, ORRs for immune checkpoint blockade in ALMM trials are only in the 10–20 % range [5], though *KIT* mutation status is not routinely substratified. Compared to European whites, ALMMs are also more common in people of non-European descent, which adds additional complexity to this disease due to genetic and environmental variations across different populations [87,88]. Thus, newer therapeutic approaches are needed for ALMMs, particularly KIT-altered melanomas.

We undertook a multiphased approach to discovering novel approaches for treating ALMMs linked to KIT mutations. We first developed an allograft system of KIT-driven murine melanoma using the most prevalent KIT mutation in human melanoma specimens- KIT^{K642E} (Kit^{K641E} in mice) [47]. This model engrafts efficiently in immunocompetent C57BL/6 mice and exhibits genetic and pharmacological features of Kit^{K641E} dependency. Robust tumorigenicity of the $mKit^{K641E}$ in C57BL/6 mice was a critical barrier in pursuing novel immunological strategies for this subgroup of melanoma. Second, in considering therapeutic engineering, we decided to pursue a biomembranous nanovaccine for several reasons. The biological component of such a nanovaccine recapitulates the major driving forces behind anti-tumor immune responses, i.e., the synaptic interactions at the cellular membranes of lymphocytes, antigen-presenting cells, and tumor cells.

Specifically, 20–200 nm sized NPs are generally taken up through endocytosis followed by successful stimulation of CD4, CD8, and T_h1-type immune responses [58]. NPs with a size of 20–200 nm can freely drain into LNs [57], whereas larger particles (<500 nm) would be predominantly taken up by peripheral APCs [89] while smaller particles (<20 nm) would be cleared by the blood and bypass LN [90]. Regarding surface charge, the interstitial fluid is comprised of negatively charged proteins; therefore, anionic NPs drain more swiftly to LN due to charge repulsion [59,60]. Additionally, cationic NPs appear more toxic than negatively charged NPs [91]. Finally, for the nano-delivery applications, PDI, a representative index for the distribution of size populations of less than 0.3, is generally accepted and specifies a homogenous population [92]. According to a previous study, similar PDI-bearing NPs have also induced robust immune responses [93]. We hypothesized that a nanoconstruct with wholesale availability of all membrane proteins from both DCs and tumor cells would more effectively identify, instruct, and incite the immune response given the entirety of the antigen presentation machinery and an entire repertoire of antigens. In addition, we cargoed an FDA-approved immunogen (e.g., imiquimod) that activates TRL7 and 8, triggering a signaling cascade that promotes the secretion of pro-inflammatory cytokines and the induction of a tumor-directed cellular immune response [94].

Simultaneous targeting of LNs and tumors can overcome drawbacks associated with individual mono-targeting of either site alone. Tumor-only targeting suffers from drawbacks like the immunosuppressive microenvironment of TME, limited immune activation (primary immune activation but not systemic activation), and the development of resistance mechanisms by tumors to evade immune recognition [95]. Similarly, LN-only targeting has the limitation of insufficient tumor eradication (activation of naïve T cells), ineffective infiltration or functionality of effector T cells, and immunosuppressive feedback with dysfunctional activated T cells after reaching the TME [96]. Dual targeting has the potential to overcome all these mono-targeting limitations with their advantages like enhanced immune activation (robust generation of CTLs by LNs targeting and effective production of effector T cells by TME targeting), improved T cell trafficking with simultaneous triggered activation and tumor infiltration, amplification of anti-tumor immune responses with generation of feedback loop enabled by release of tumor antigens and enhancement of APCs in LNs boosting immune cell activation, and preventing immune exhaustion [97]. Nanomedicine has the potential of dual targeting similar to bifunctional antibodies targeting tumor antigens/activating co-stimulatory pathways in LNs and cellular therapy like CAR-T retaining activity in both LNs and TME [98].

We used a panel of in vitro and in vivo assays to unravel the HBNV's immune effects. Using SRB as cargo, we found that adding the biomembranous coat enhanced both cellular uptake in vitro and iLN and tumor homing in vivo. Prior studies have shown that BNPs are taken up through energy-dependent receptor-mediated endocytosis [99] and that cancer cell BNPs exhibit homotypic targeting in vitro [99,100]. Our in vitro experiments showed that the presence of a hybrid membrane allowed for dual Kit_{C3}^{K641E} cell and DC targeting (Fig. 2a), while our in vivo studies (Fig. 4) demonstrate successful uptake of the HBNVs by iLN DCs and selective organ and tumor homing (Fig. 4b). While the precise mechanism of this homing has yet to be explored, the presence of membrane proteins from both the DCs and Kit_{C3}^{K641E} cells (e.g., MHC, adhesion, co-stimulatory molecules as well as chemokine receptors) likely influenced proper homing [48]. The differential enrichment of the DC-only NV (i.e., DBNV) within the iLNs and the Kit_{C3}^{K641E} -only NV (i.e., KBNV) within the tumor further supports a homotypic interaction [101]. Beyond homing, anti-tumor immune responses were also interrogated using a battery of in vitro and in vivo studies. While free imiquimod and PIPNPs did show some immunostimulation, the HBNV substantially enhanced the maturation of DCs, stimulation of $CD8^+$ T cells, and a reduction of Tregs. Lastly, the primary endpoint of our study was to demonstrate the efficacy of the novel HBNV. In both the therapeutic and prophylactic trials, HBNVs significantly reduced tumor formation compared to control and both free and encapsulated imiquimod, thus meeting our endpoints. While we did observe a maturation of DCs and an increase of $CD8^+$ cells in the draining iLN from HBNV vaccination, more detailed studies are underway to examine the dynamic nature of the immune response in both LNs and tumor specimens at various timepoints after HBNV exposure.

Prior studies of cancer cell membrane-coated nanoparticles using single B16 melanoma membranes demonstrated successful C57BL/6 DC maturation [100] and prophylactic tumor prevention against B16F10 tumor challenge [8]. In one study, imiquimod-loaded BNVs conjugated with mannose-modified membranes from B16-OVA cells [102] showed significant tumor suppression when added to anti-PD1. However, in contrast to these single membrane approaches, we believe that a hybrid membrane can be leveraged for better homing and immune stimulation.

Moreover, the use of the foreign OVA antigen may produce immunological artifacts absent with native TAAs from the Kit_{C3}^{K641E} cell.

Molecular profiling of the tumor specimens revealed several interesting findings. Hierarchical clustering using deconvoluted immune cell phenotyping revealed three classes of tumor infiltration. These classes may reflect distinct eradicative mechanisms, a temporal phenomenon whereby there is a downregulation of immune infiltration after the initial HBNV-mediated tumor response, immune cell exhaustion, or a sampling issue whereby tumor inflammation was underrepresented in the RNA-sequenced zone. Our current analyses allow us to delineate molecularly, but not decipher mechanistically, the underpinnings of this class structure. Our analysis also showed that HBNV treatment induced a robust immune reaction predominated by B cell responses, though there was also significant enrichment for $CD8^+$ cells. The presence of these populations raises the possibility of tertiary lymphoid structures (TLS) being generated by the HBNV. TLS have been shown to play significant roles in the immune response against melanoma, particularly in enhancing immune activity and improving patient outcomes. In metastatic melanoma samples, the presence of both $CD8^+$ T cells and $CD20^+$ B cells correlate with improved survival, independent of other clinical variables. Immunofluorescence staining of CXCR5 and CXCL13 with CD20 shows TLS formation in these $CD8^+CD20^+$ tumors. A TLS-associated gene signature predicted clinical outcomes in patients treated with checkpoint blockade. B-cell-rich tumors also had increased levels of $TCF7^+$ naive and/or memory T cells, while tumors lacking TLS exhibited a dysfunctional T cell phenotype [82]. While we did not observe histological evidence of TLS in our tumors, elements of TLS gene signatures were recovered from our RNAseq data. TLS formation in melanoma is partly orchestrated by cancer-associated fibroblasts and involves $CD8^+$ T cells and CXCL13-mediated recruitment of B cells, facilitating immune cell infiltration and organization [103]. In terms of the cargo, imiquimod and its analog R-848 have been shown to induce the proliferation of murine and human B cells and stimulate immunoglobulin production [104]. Combinations to enhance tumor response with concomitant use of other immunomodulators and checkpoint inhibitors are currently being explored. TMB.

The HBNV nanoconstruct has several potential advantages over current FDA-approved therapeutic cancer vaccines such as BCG and sipuleucel-T [105]. Sipuleucel-T uses a prostate cancer-selective TAA-prostatic acid phosphatase [106]. With a single antigen vaccine like sipuleucel-T, heterogeneity within the tumor and loss of antigen expression could lead to immune escape. In contrast, a hybrid membrane confers the full spectrum of antigens (both TAAs and TSAs) available from the cancer cell and endogenous MHC molecules from the DCs, which can promote a broader T cell repertoire [8]. Such is also the case with personalized cancer vaccines, which incorporate multiple TSAs based on predicted missense mutations [107] and have shown significant survival benefit in the trial setting [108]. In addition, the marked success of therapies based on whole spectrum tumor antigenicity, including immune checkpoint inhibition [109] (and TIL therapy [110], further suggest that single antigen approaches may not necessarily constitute the ideal anti-cancer vaccine.

There are several limitations to our studies and the nanotechnology more broadly. First, given our interest in *KIT*-altered melanomas, this proof-of-concept fabrication used a single avatar of the most encountered c-Kit mutation in human melanoma. Additional murine melanoma lines that mimic human mutations are currently underway. Given its uncertain relevance to human melanoma genetics, we elected not to pursue the B16 model. Second, as alluded to above, the fundamental nature of the biomimesis is to replicate all possible surface antigens. Thus, the precise epitopes that engendered the anti-tumor immune response are not known. Third, in these early phase trials, we focused on the efficacy of the HBNV alone and the series of control formulations. The use of known clinical agents, such as imatinib and anti-PD1 antibodies, are currently being incorporated into downstream trials. Fourth, biomimetic nanoconstructs present significant challenges due to the complexity of their membrane structures. The diversity of membrane molecules makes it difficult to pinpoint critical moieties for their observed physiological effects. Additionally, the surface protein or moieties mediating the selective homing to tumor vs. iLN is currently unknown. Efforts to block individual membrane proteins have been limited and complicated by potential functional redundancy among proteins or unexpected contributions from less-studied proteins. The isolation of key proteins may play a larger role in the scalability of the NP design. Fifth, despite the focus on surface proteins, the roles of the phospholipid bilayer and membrane-associated carbohydrates are underexplored and could offer new avenues for developing biomimetic systems. Lastly, regulatory challenges also arise from the biological origins of these materials, necessitating specific guidelines for their validation and use in biomedical applications. Understanding the interactions between membrane components and the biological environment is crucial for advancing biomimetic technology in a tailored and safe design environment.

In conclusion, we have leveraged a novel murine model of treatment-resistant *KIT*-activated melanomas to address an unmet therapeutic need. The HBNV is a proof-of-concept nanoconstruct that integrates the biomachinery of an "artificial" DC along with the cargo space for immune adjuvants. Ongoing research is focusing on the combinatorial flexibility of combining genetic engineering with small molecule discovery to maximize the immunostimulatory effects of biomimetic nanoparticles.

4. Materials and methods

4.1. Cells, materials, and mice

KIT_{C3}^{K641E} cells, dendritic cells (DCs, immortalized DC2.4, Millipore, MA), and fused cells were cultured in Roswell Park Memorial Institute (RPMI-1640) medium (Gibco, Waltham, MA) supplemented with 10 % fetal bovine serum (FBS) (Gibco, Waltham, MA) and 1X Antibiotic-Antimycotic (Thermo Fisher Scientific, Waltham, MA). Acid-capped poly(D,L-lactide-co-glycolide) (PLGA, 10k, D,L-LA/GA = 50:50) was procured from Nanosoft Polymers (Winston-Salem, NC). Poly(vinyl alcohol) (PVA) and polyethyleneimine (PEI) were purchased from Sigma-Aldrich (St. Louis, MO). Mem-PER™ Plus Membrane Protein Extraction Kit and Wheat Germ Agglutinin, Alexa Fluor™ 488 Conjugate was purchased from Thermo Fisher Scientific (Waltham, MA). Imiquimod (IMQ) was purchased from MedChemExpress LLC (Monmouth Junction, NJ). The Extruder Set was purchased from Avanti Polar Lipids (Alabaster, AL).

The Institutional Animal Care and Use Committee at Massachusetts General Hospital approved all mice trials. C57BL/6J mice aged 5–6 weeks (male and female) were acquired from Jackson Laboratory (Bar Harbor, ME).

4.2. Fusion and fabrication

Fusion of the DC and Kit_{C3}^{K641E} was performed first by making the Kit_{C3}^{K641E} inactive and hybridization was performed according to the previous reports with some alterations [28,48,49,111]. The inactive Kit_{C3}^{K641E} and DCs were mixed in a tube at a 1:1 ratio (number of cells), and the mixture was centrifuged (500 g, 10 min) with the brake and acceleration deactivated. Subsequently, a pre-warmed solution containing 50 % polyethylene glycol (PEG, M.W.: 4000, w/w) and 10 % dimethyl sulfoxide (DMSO) was incrementally added to the cell pellet over the duration of 1 min and gently vortexed to ensure homogeneity. The resultant mixture was then incubated at 37 °C for 2 min in a water bath. This was followed by a gradual addition of FBS-free RPMI 1640 media. A final centrifugation step was performed, and the pellet containing hybridized cells was resuspended in RPMI 1640 media and cultured under standard conditions (37 °C, 5 % CO2) with 10 % FBS and 1 % antibiotic supplement for subsequent experiments.

Blank PLGA NPs (PNPs) and IMQ-loaded PNPs (IPNPs) were prepared using the oil-in-water (o/w) single-emulsion method following the previous report [112] with some alterations. PLGA (Nanosoft Polymers, Winston-Salem, NC) was dissolved in dichloromethane and acetone (50:50, 5 mg/mL), whereas IMQ (MedChemExpress LLC, Monmouth Junction, NJ) was dissolved in DMSO (2.5 mg/mL). 45 μL of IMQ was added to 1 mL of PLGA. Subsequently, 1 mL of PVA (1 % w/v, Sigma-Aldrich, St. Louis, MO) was added to the stirring mixture dropwise and sequentially vortexed (for 10 s), bath sonicated (for 30 s), and probe sonicated (60 % amplitude, 1 min, 5s "on" and 5 s "off" pulse). Next, 3 mL of PVA (1 % w/v) was added to the homogenized solution with continuous stirring and sonicated with similar settings. The solution was vortexed for 10 s and stirred for 4 h to evaporate the organic solvent at room temperature. IPNPs were prepared after separating the microparticle pellet with centrifugation (4500 rpm, 5min) and subjecting the supernatant for centrifugation (7500 rpm, 5min). PNPs were prepared following a similar method, eliminating the step of IMQ loading.

PEI (25 kDa, 200 μL, Sigma-Aldrich, St. Louis, MO) was added to the IPNPs to form PEI-capsuled IPNPs (PIPNPs). Then, the mixture was vortexed, probe sonicated with similar settings, stirred for 30 min, and centrifuged as mentioned above. PEI-capsuled PNPs were prepared similarly to PIPNPs, bypassing the IMQ loading step. The membrane proteins from the cells were isolated following the manufacturer's instructions of Mem-PER™ Plus Membrane Protein Extraction Kit (Thermo Fisher Scientific, Waltham, MA) and described schematically (Fig. S1). The membrane proteins (125 μg) were integrated into the PIPNPs with vortexing (for 10 s), bath sonication (for 30 s), and probe sonication (60 % amplitude, 1 min, 5s "on" and 5 s "off" pulse). Finally, the solution was passed through the mini-extruder system (Avanti Polar Lipids, Alabaster, AL) using a filter of 200 nm to form HBNVs. Then, the solution was freeze-dried and stored at −20 °C for further experiments. DBNVs and KBNVs were prepared following the similar protocol of HBNVs, just replacing the steps of the membrane proteins of fused cells with DCs and Kit_{C3}^{K641E} cells, respectively.

4.3. Characterization

The morphological characterization was performed through transmission electron microscopy (TEM, Philips CM-10, Andover, MA) by dropping the solution of the NPs on carbon-coated copper grids, staining with 2 % phosphotungstic acid, drying, and observing under the microscope.

The particle size, poly-dispersity index (PDI), and surface charge/zeta potential were analyzed through the Zetasizer Nano instrument (Malvern Panalytical Ltd., Grovewood Road, U.K.). The loading capacity (L.C.) and entrapment efficiency (E.E.) of the IMQ and membrane protein were analyzed from liquid chromatography–mass spectrometry (LC-MS, Agilent 1290 Infinity, Santa Clara, CA) and DC (detergent compatible) protein assay kit (Bio-rad, Hercules, CA). L.C. was calculated based on the amount of payload to nanoformulation whereas E.E. was calculated based on the loaded amount to the initial loading. The stability of the nanoparticles was analyzed with the examination of particle size, PDI, and zeta potential on different days after fabrication with storage of the NPs at 4 °C.

The presence of glycosylated proteins in the different forms of nanoformulations was analyzed using the wheat germ agglutinin (WGA) assay [113]. Briefly, WGA conjugated at 1 μg/mL Alexa Fluor 488 (Thermo Fisher Scientific, Waltham, MA) in HBSS solution was incubated for 10 min with PIPNPs (negative control), tumor membrane proteins (positive control), and HBNVs. The unreacted WGA was eliminated using 300 kDa MWCO ultrafiltration Vivaspin tubes (Sartorius). Using a Fluorescence Microplate Reader (Spectramax M5, Molecular Devices, San Jose, CA), the WGA fluorescence intensity was measured at an excitation/emission of 495/519 nm.

Membrane protein profiles of cells, PIPNPs, and HBNVs were analyzed through crystal violet staining. After quantifying the membrane proteins' concentration from the DC protein assay kit, the proteins, PIPNPs, and HBNVs (with membrane proteins) were mixed with protein sample buffer, heated to 95 °C (5 min), and loaded (10 μL) into wells for SDS-PAGE (10 %) and molecular weight marker was also loaded simultaneously. Further, the protein samples were separated at 100–120V for 1–2 h. For crystal violet staining, the protein samples subjected to the SDS page were exposed to 0.001 % (w/v) of crystal violet (in 10 % v/v methanol and 1.5 % v/v acetic acid) staining. Two washes of 5 % (v/v) methanol in dH_20 were performed on SDS-PAGE gel (15 min). The staining gel was preheated to 60 °C to shorten the staining time. After 30 min, the images were taken when the background was clear.

2×10^5 cells were seeded on a well (12-well plates) with coverslips, cultured for 24 h, and incubated with FITC anti-mouse CD11c (Biolegend, San Diego, CA) and P.E. anti-mouse CD117 (c-kit) (Biolegend, San Diego, CA) antibodies. After 15 min, the cells were washed, fixed with 4 % polyformaldehyde (BM-155, Boston BioProducts), and stained with 4, 6-diamidino-2-phenylindole (DAPI) to stain the nucleus. Next, all images were then taken with confocal laser scanning microscopy (CLSM) to characterize the cell surface marker expression in individual and fused cells.

4.4. Uptake, cytokine release, and maturation assay

Using flow cytometry and CLSM, the intracellular fluorescence intensity of Sulforhodamine-B (SRB)-conjugated nanoformulations in individual and fused cells was to estimate the cellular internalization of nanoformulations. Cells (12-well plates, 2×10^5/well) were treated with the various nanoformulations for 1 h at an SRB concentration of 0.5 μg/mL, washed twice using PBS, and then subjected to flow cytometry using the BD FACSARIA Cell Analysis System (B.D. Biosciences, San Jose, CA). The uptake was also examined with CLSM. Cells were seeded on the well plate with the coverslips, washed twice with PBS, and fixed with 4 % paraformaldehyde for 10 min. Treated cells were stained with DAPI to identify the nuclei and washed to remove the background fluorescence. Images were taken with a confocal microscope.

2×10^3 cells were seeded on a well (96-well plates), cultured for 24 h, and exposed to PBS (control), free IMQ (0.5 μg/mL), and NPs (PPNPs, PIPNPs, and HBNVs), using equivalent concentrations of IMQ and tumor membrane proteins (0.5 μg/mL). After 48 h of treatment, the supernatant was used for further assessment. Cytokine release assays were performed using the Mouse TNF Alpha/Tumor Necrosis Factor enzyme-linked immunosorbent assay (ELISA) Kit PicoKine, Mouse IL-6/Interleukin-6 ELISA Kit PicoKine, Mouse IL-12(P40) ELISA Kit PicoKine, and Mouse IL-10/Interleukin-10 ELISA Kit PicoKine from Boster Bio (Pleasanton, CA) following the manufacturer's instructions.

Using 10^6 cells/well, immature DCs were seeded onto 6-well plates and incubated with PBS (control), free IMQ (0.5 μg/mL), and NPs (PPNPs, PIPNPs, and HBNVs) and exposed to equivalent concentrations of IMQ and tumor membrane proteins (0.5 μg/mL) for 48 h. After harvesting, the DCs were washed with PBS and stained with PerCP-Cy5.5 anti-mouse CD86 antibody, APC anti-mouse CD80 (Biolegend, San Diego, CA), and FITC anti-mouse CD11c (Biolegend, San Diego, CA) antibodies. Then, after washing twice, the cells were analyzed through a flow cytometer to characterize maturation.

4.5. Biodistribution, activation, and maturation

The biodistribution of the free SRB, SRB-loaded PIPNPs, and SRB-loaded HBNVs was assessed and compared after the subcutaneous administration to the tail base of C57BL/6 mice. An ex-vivo analysis evaluation of different organs was performed using protocols from previous reports [25,114]. 24 h after SRB and NP administration, the inguinal lymph node (iLN), heart, liver, lungs, spleen, and kidneys were removed and examined for fluorescence in the vital organs using the

IVIS Lumina Series III imaging instrument. In vivo atability of the HBNVs was examined with analysis of ex vivo fluorescence after 48 h and 72 h.To better elucidate the targeting ability of HBNVs compared with PIPNPs at the single cell level, iLNs were isolated and digested using Collagenase D (Sigma-Aldrich, St. Louis, MO) and DNAse I (Thermo Fisher Scientific, Waltham, MA) in a shaking incubator (37 °C, 30 min). Then, the digested samples were passed through a 70-μm cell strainer (Sigma-Aldrich, St. Louis, MO) to obtain single cells. The single cells were also analyzed through flow cytometry by SRB fluorescence, whereas the DC-homing ability was analyzed through staining of FITC anti-mouse CD11c (Biolegend, San Diego, CA) antibody and SRB fluorescence. Similarly, in the Kit_{C3}^{K641E} inoculated C57BL/6 mice, TME homotypic targeting was assessed with additional examination of tumors and all other vital organs using the same protocol listed above.

The EasySep Mouse $CD8^+$ T Cell Isolation Kit (Stemcell Technologies, Vancouver, Canada) was utilized to isolate naïve $CD8^+$ T cells from the splenocytes of 6-to 8-week-old female C57BL/6 mice. The eBioscience protein transport inhibitor cocktail (Thermo Fisher Scientific, Waltham, MA) was added to the harvested $CD8^+$ T cells, and the DCs that had been pre-treated with PBS (control), free IMQ (0.5 μg/mL), and various NPs (PPNPs, PIPNPs, and HBNVs), where equivalent concentrations of IMQ, and tumor membrane proteins (0.5 μg/mL) were added. Following a 72 h treatment period, the $CD8^+$ T cells were isolated and labeled using APC anti-mouse CD8a and P.E. anti-mouse CD3 (Biolegend, San Diego, CA) antibodies. Then, they were fixed and permeabilized using an intracellular Fixation & Permeabilization Buffer Set (Thermo Fisher Scientific, Waltham, MA) per the manufacturer's instructions. The cells were examined with flow cytometry after staining with Pacific Blue anti-mouse IFN-γ antibody (Biolegend, San Diego, CA). Similarly, harvested $CD8^+$ T cells, and the DCs that had been pre-treated with PBS (control), free IMQ (0.5 μg/mL), and various NPs (PPNPs, PIPNPs, and HBNVs), where the equivalent concentrations of IMQ, and tumor membrane proteins (0.5 μg/mL) were co-cultured for 48 h at 37 °C in the incubator. After harvesting, cells were treated with fluorescent-labeled antibodies (APC anti-mouse CD8a and P.E. anti-mouse CD25 Antibody) for 30 min at 4 °C (BioLegend, San Diego, USA). Cells were examined for markers of T cell activation using flow cytometry; double-positive (CD8 and CD25) cells were gated, and the results were expressed as a percentage of positive cells.

In vivo DC maturation assay was performed 72 h after administration of PBS (control), free IMQ (0.5 μg/mL), and various NPs (PPNPs, PIPNPs, and HBNVs). Tumor-draining iLNs were isolated and digested as described above to obtain the single cells. Then, the single cell suspensions were incubated with APC anti-mouse CD86 antibody, P.E. anti-mouse CD80 (Biolegend, San Diego, CA), and FITC anti-mouse CD11c (Biolegend, San Diego, CA) antibodies. Finally, the cells were washed and subjected to flow cytometric analysis.

4.6. Prophylactic and therapeutic anti-tumor study

Animal studies. All animal studies were approved by the Institutional Animal Care and Use Committee at Massachusetts General Hospital (MGH). C57/BL6 mice were housed in the BL2 animal facility at MGH. For the prophylactic study, 5–6-week-old male and female C57BL/6 mice were subcutaneously immunized twice (on −28 d and −21 d) with PBS (control), 10 μg of IMQ, and different NPs at equivalent concentrations of membrane proteins and IMQ (10 μg). Kit_{C3}^{K641E} cells were resuspended in PBS (5×10^6 cells per mL) and injected subcutaneously (5×10^5 cells/100 μL/mouse) into the right flank of 7–8-week-old male and female C57BL/6 mice 7 days of the second immunization (i.e. −14 d). For the therapeutic study, 5×10^5 Kit_{C3}^{K641E} cells were resuspended in PBS (5×10^6 cells per mL) and injected into the right flank of the 6-7-week-old male and female C57BL/6 mice (day −14). About 14 days after injection when the tumors reached ~100 mm^3, the mice were randomly separated into different groups (day 0). The mice were immunized 3 times every 4 days (0 d, 4 d, and 8 d) with PBS (control), 10 μg of IMQ, and different NPs at equivalent concentrations of membrane proteins and IMQ (10 μg). During the study period, the tumor's length (long dimension) and width (short dimension) were measured using an electronic digital caliper to determine the tumor volume with the formula of half of the product of the square of tumor width and length. Tumor volume and body weight were measured every four days, survival of mice was also studied simultaneously every day.

Tissue examination. Histological examination of the formalin-fixed and paraffin-embedded section of tissues of vital organs (heart, liver, lungs, spleen, kidneys, and lymph nodes) was performed. The sections were also subjected to hematoxylin and eosin (H&E) staining for general histopathological profiles to study toxicity associated with NPs after the prophylactic study with isolated organs. For biological TEM (Bio-TEM), tumor-bearing C57BL/6 mice were sacrificed after treatment with PBS (control), HBNVs (subcutaneous), and HBNVs (intratumoral, I.T.). Subsequently, their tumors and iLNs were removed for Bio-TEM analysis. TEM was then used to image the acquired sections after they had been stained with uranyl acetate/lead citrate staining. The isolated tumors and iLNs from control and treated mice were also fixed in the formalin, and sections of those tissues in the slides were incubated with PE anti-mouse CD8a (Biolegend, San Diego, CA) antibody. After 15 min, the cells were washed and then, it was fixed with 4 % polyformaldehyde (BM-155, Boston BioProducts) and stained with 4, 6-diamidino-2-phenylindole (DAPI) to stain the nucleus. Next, all images were then taken with confocal laser scanning microscopy (CLSM) to characterize the expression of CD8 in tumors and iLNs.

Tumor cell analysis. As described in a previous report [74], the tumor cell suspension was generated to examine the intra-tumoral profiles of immune cells. After the tumor pieces were crushed and homogenized with a 10 mL syringe plunger in the digestion medium as mentioned above, the tumor suspensions were filtered through 70 μm cell strainers measuring to eliminate any remaining undigested tissue. The single cells were gathered, the supernatants were disposed of, and the cells were centrifuged at 800×*g* for 5 min at 4 °C. Red blood cell (RBC) lysis buffer was added to the cell pellets and incubated on ice for 5 min to deplete the RBC in the tumor cell suspension. After adding the RPMI medium to neutralize the lysis buffer, cells were harvested by centrifugation at 800×*g* for 5 min at 4 °C. To inhibit the Fc receptor, the RBC-depleted tumor single cells were treated with (1.0 μg/10^6 cells/100 μl) anti-mouse CD16/CD32 antibody (Biolegend, San Diego, CA) for 20 min on ice. The resulting cell suspensions were stained with P.E. anti-mouse CD3 and APC anti-mouse CD8a to quantify the number of CD8 T cells in tumors. $CD4^+$ T cells were quantified with P.E. anti-mouse CD3 and FITC anti-mouse CD4 antibodies (Biolegend, San Diego, CA). The eBioscienceTM Foxp3/Transcription Factor Fixation/Permeabilization kit (ThermoFisher Scientific) and APC/Cy7 anti-mouse Foxp3 antibody (Biolegend, San Diego, CA) were used to determine the number of regulatory T cells (Tregs) in the tumors. Similarly, M1 phenotype macrophages ($CD80^+CD11b^+F4/80^+$) and M2 phenotype macrophages ($CD206^+CD11b^+F4/80^+$) in the tumors were also analyzed after staining with FITC anti-mouse CD11b, P.E. anti-mouse F4/80, APC anti-mouse CD80, and APC/Cy7 anti-mouse CD206 antibodies (Biolegend, San Diego, CA) by flow cytometry.

4.7. Bulk tumor RNA seq

RNAseq was performed by Admera Health (South Plainfield, NJ) using the Illumina 2x150 sequencer with a sequencing Output of 40M total reads per sample (20M in each direction). Below is a brief summary of the pipeline from Admera Health.

RNA Extraction and Q.C. RNA was purified from 25 mg of tumor sample using the RNeasy Plus Mini Kit. Isolated RNA sample quality was assessed by RNA Tapestation (Agilent Technologies Inc., California, USA) and quantified by AccuBlue® Broad Range RNA Quantitation assay (Biotium, California, USA).

NEBNext Ultra II RNA with PolyA Selection. Paramagnetic beads

coupled with oligo d(T)25 are combined with total RNA to isolate poly (A) + transcripts based on NEBNext® Poly(A) mRNA Magnetic Isolation Module manual (New England BioLabs Inc., Massachusetts, USA). Prior to first strand synthesis, samples are randomly primed (5′ d(N6) 3' [N = A,C,G,T]) and fragmented based on the manufacturer's recommendations. The first strand is synthesized with the Protoscript II Reverse Transcriptase with a longer extension period, approximately 30 min at 42 °C. All remaining steps for library construction were used according to the NEBNext® Ultra™ II Directional RNA Library Prep Kit for Illumina® (New England BioLabs Inc., Massachusetts, USA). Final library quantities were assessed by Qubit 2.0 (ThermoFisher, Massachusetts, USA), and quality was assessed by TapeStation HSD1000 ScreenTape (Agilent Technologies Inc., California, USA). Final library size was about 450bp with an insert size of about 300bp. Illumina® 8-nt dual-indices were used. Equimolar pooling of libraries was performed based on Q. C. values and sequenced on an Illumina NovaSeq X Plus 10B (Illumina, California, USA) with a read length configuration of 150 PE for 40M PE reads per sample (20M in each direction).

Data Analysis. FastQC (version v0.12.1) was employed to check the quality of raw reads. Trimmomatic (version v0.39) was applied to cut adaptors and trim low-quality bases with default setting. STAR Aligner (version 2.7.10b) was used to align the reads. The package of Picard tools (version 3.0.0) was applied to mark duplicates of mapping. StringTie (version 2.2.1) was used to assemble the RNA-Seq alignments into potential transcripts. FeatureCounts (version 2.0.6) or HTSeq (version 2.0.3) was used to count mapped reads for genomic features such as genes, exons, promoter, gene bodies, genomic bins, and chromosomal locations. DESeq2 (version 1.40.2) was employed to process the differential gene expression analysis. The gene ontology (GO), gene set enrichment analysis (GSEA), and KEGG enrichment analysis were analyzed via the ClusterProfiler package and Molecular Signatures Database. (MSigDB). The protein-protein interaction networks and functional enrichment analysis were processed via the R tool "STRINGdb" (version 2.10.1). The ANOVA analysis was implemented by the edgeR R package (version 3.28.1). Additional analyses were also performed using Webgestalt (https://www.webgestalt.org/).

4.8. Statistical analysis

The mean ± S.D. is used to express the findings. GraphPad Prism 10.1.2 (GraphPad Software, San Diego, CA) was used for the statistical analysis and graphing. Student's t-test was utilized to ascertain statistically significant differences between two groups. One-way ANOVA and two-way ANOVA with Tukey's multiple comparisons were used to identify significant differences between more than two groups and multiple comparisons of the tumor volume of mice during the study period. A significant statistical difference was defined as $^{*}p < 0.05$. Utmost significant differences were defined as: $^{*}p < 0.05$, $^{**}p < 0.01$, $^{***}p < 0.001$, and $^{****}p < 0.0001$.

CRediT authorship contribution statement

Kishwor Poudel: Writing – review & editing, Writing – original draft, Visualization, Validation, Software, Project administration, Methodology, Investigation, Formal analysis, Data curation, Conceptualization. **Zhenyu Ji:** Validation, Software, Methodology, Formal analysis, Data curation. **Ching-Ni Njauw:** Methodology, Investigation. **Anpuchchelvi Rajadurai:** Methodology, Investigation. **Brijesh Bhayana:** Methodology, Investigation. **Ryan J. Sullivan:** Writing – review & editing, Validation, Supervision. **Jong Oh Kim:** Writing – review & editing, Validation, Supervision. **Hensin Tsao:** Writing – review & editing, Visualization, Validation, Supervision, Software, Resources, Project administration, Methodology, Funding acquisition, Formal analysis, Data curation, Conceptualization.

Ethics approval and consent to participate

Protocols involved in the use of animals were reviewed and approved by the Institutional Animal Care and Use Committee at Massachusetts General Hospital. All experiments followed the approved protocols (Approval Protocol No. 2017N000228).

Declaration of competing interest

The authors declare that they have no known competing financial interests or personal relationships that could have appeared to influence the work reported in this paper.

Acknowledgements

The authors appreciate the efforts from Dr. Jie Zhao, and technical assistants, Danian Cao and Neema Kumar for performing Electron Microscopy, FACS, and H&E staining (MGH). The authors also appreciate the efforts from MGH-IACUC for animal care. The graphical abstract and scheme of Fig. 1 were drawn using Biorender.com. This work was supported by Richard Allen Johnson, MD Endowed Chair in Dermatology (to H.T.), and Melanoma Research Alliance (to H.T.), and the Department of Defense (Award HT9425-24-1-0930 to H.T.).

Appendix A. Supplementary data

Supplementary data to this article can be found online at https://doi.org/10.1016/j.bioactmat.2024.12.023.

References

[1] D. Meng, R.D. Carvajal, KIT as an oncogenic driver in melanoma: an update on clinical development, Am. J. Clin. Dermatol. 20 (3) (2019) 315–323.
[2] F. Newell, et al., Comparative genomics provides etiologic and biological insight into melanoma subtypes, Cancer Discov. 12 (12) (2022) 2856–2879.
[3] N.K. Hayward, et al., Whole-genome landscapes of major melanoma subtypes, Nature 545 (7653) (2017) 175–180.
[4] J. Zhang, et al., Treatment of acral and mucosal melanoma: current and emerging targeted therapies, Crit. Rev. Oncol. Hematol. 193 (2024) 104221.
[5] A. Fortuna, T. Amaral, Multidisciplinary approach and treatment of acral and mucosal melanoma, Front. Oncol. 14 (2024) 1340408.
[6] J. Xu, et al., A general strategy towards personalized nanovaccines based on fluoropolymers for post-surgical cancer immunotherapy, Nat. Nanotechnol. 15 (12) (2020) 1043–1052.
[7] T. Wang, et al., A cancer vaccine-mediated postoperative immunotherapy for recurrent and metastatic tumors, Nat. Commun. 9 (1) (2018) 1532.
[8] J. Zhou, et al., Biomimetic nanotechnology toward personalized vaccines, Adv. Mater. 32 (13) (2020) e1901255.
[9] Z. Hu, P.A. Ott, C.J. Wu, Towards personalized, tumour-specific, therapeutic vaccines for cancer, Nat. Rev. Immunol. 18 (3) (2018) 168–182.
[10] W.H. Li, Y.M. Li, Chemical strategies to boost cancer vaccines, Chem. Rev. 120 (20) (2020) 11420–11478.
[11] T.N. Schumacher, R.D. Schreiber, Neoantigens in cancer immunotherapy, Science 348 (6230) (2015) 69–74.
[12] Y.C. Lu, P.F. Robbins, Cancer immunotherapy targeting neoantigens, Semin. Immunol. 28 (1) (2016) 22–27.
[13] Y. Jiang, et al., Engineered cell-membrane-coated nanoparticles directly present tumor antigens to promote anticancer immunity, Adv. Mater. 32 (30) (2020) e2001808.
[14] I. Trenevska, D. Li, A.H. Banham, Therapeutic antibodies against intracellular tumor antigens, Front. Immunol. 8 (2017) 1001.
[15] N. Vigneron, Human tumor antigens and cancer immunotherapy, BioMed Res. Int. 2015 (2015) 948501.
[16] J. Pitcovski, et al., Melanoma antigens and related immunological markers, Crit. Rev. Oncol. Hematol. 115 (2017) 36–49.
[17] D. Hudrisier, et al., The efficiency of antigen recognition by CD8+ CTL clones is determined by the frequency of serial TCR engagement, J. Immunol. 161 (2) (1998) 553–562.
[18] Y. Liao, et al., Biomimetic hybrid membrane-based nanoplatforms: synthesis, properties and biomedical applications, Nanoscale Horiz 5 (9) (2020) 1293–1302.
[19] C. Yang, et al., Leveraging senescent cancer cell membrane to potentiate cancer immunotherapy through biomimetic nanovaccine, Adv. Sci. 11 (30) (2024) 2400630.
[20] Z. Zhong, et al., Cell membrane coated nanoparticles as a biomimetic drug delivery platform for enhancing cancer immunotherapy, Nanoscale 16 (18) (2024) 8708–8738.

[21] Y. He, et al., Intravenous senescent erythrocyte vaccination modulates adaptive immunity and splenic complement production, ACS Nano 18 (1) (2024) 470–482.
[22] M.J. Lin, et al., Cancer vaccines: the next immunotherapy frontier, Nat. Can. (Ott.) 3 (8) (2022) 911–926.
[23] R. Zhang, M.M. Billingsley, M.J. Mitchell, Biomaterials for vaccine-based cancer immunotherapy, J. Contr. Release 292 (2018) 256–276.
[24] D. Hudrisier, et al., The efficiency of antigen recognition by $CD8^+$ CTL clones is determined by the frequency of serial TCR engagement, J. Immunol. 161 (2) (1998) 553–562.
[25] C.D. Phung, et al., Nanovaccines silencing IL-10 production at priming phase for boosting immune responses to melanoma, J. Contr. Release 338 (2021) 211–223.
[26] C. Yang, et al., Biomimetic nanovaccines potentiating dendritic cell internalization via CXCR4-mediated macropinocytosis, Adv. Healthcare Mater. 12 (5) (2023) 2202064.
[27] S.C. Eisenbarth, Dendritic cell subsets in T cell programming: location dictates function, Nat. Rev. Immunol. 19 (2) (2019) 89–103.
[28] J. Gong, et al., Induction of antitumor activity by immunization with fusions of dendritic and carcinoma cells, Nat. Med. 3 (5) (1997) 558–561.
[29] S. Koido, et al., Dendritic cells fused with allogeneic colorectal cancer cell line present multiple colorectal cancer–specific antigens and induce antitumor immunity against autologous tumor cells, Clin. Cancer Res. 11 (21) (2005) 7891–7900.
[30] S. Koido, et al., Fusions between dendritic cells and whole tumor cells as anticancer vaccines, OncoImmunology 2 (5) (2013) e24437.
[31] C.-X. Li, et al., Artificially reprogrammed macrophages as tumor-tropic immunosuppression-resistant biologics to realize therapeutics production and immune activation, Adv. Mater. 31 (15) (2019) 1807211.
[32] A. Sébastien, et al., Dendritic cells as pharmacological tools for cancer immunotherapy, Pharmacol. Rev. 67 (4) (2015) 731.
[33] Z. Chen, Z. Wang, Z. Gu, Bioinspired and biomimetic nanomedicines, Accounts Chem. Res. 52 (5) (2019) 1255–1264.
[34] P. Zhang, et al., Genetically engineered liposome-like nanovesicles as active targeted transport platform, Adv. Mater. 30 (7) (2018) 1705350.
[35] C.-M.J. Hu, et al., Nanoparticle biointerfacing by platelet membrane cloaking, Nature 526 (7571) (2015) 118–121.
[36] X. Liu, et al., Vesicular antibodies: a bioactive multifunctional combination platform for targeted therapeutic delivery and cancer immunotherapy, Adv. Mater. 31 (17) (2019) 1808294.
[37] P. Zhang, et al., Virus-mimetic nanovesicles as a versatile antigen-delivery system, Proc. Natl. Acad. Sci. USA 112 (45) (2015) E6129–E6138.
[38] X. Liu, et al., Bioinspired artificial nanodecoys for hepatitis B virus, Angew. Chem. Int. Ed. 57 (38) (2018) 12499–12503.
[39] S.P. Kasturi, et al., Programming the magnitude and persistence of antibody responses with innate immunity, Nature 470 (7335) (2011) 543–547.
[40] I. Le Mercier, et al., Tumor promotion by intratumoral plasmacytoid dendritic cells is reversed by TLR7 ligand treatment, Cancer Res. 73 (15) (2013) 4629–4640.
[41] J.M. Anderson, M.S. Shive, Biodegradation and biocompatibility of PLA and PLGA microspheres, Adv. Drug Deliv. Rev. 64 (2012) 72–82.
[42] F. Danhier, et al., PLGA-based nanoparticles: an overview of biomedical applications, J. Contr. Release 161 (2) (2012) 505–522.
[43] M.B. Heo, M.Y. Cho, Y.T. Lim, Polymer nanoparticles for enhanced immune response: combined delivery of tumor antigen and small interference RNA for immunosuppressive gene to dendritic cells, Acta Biomater. 10 (5) (2014) 2169–2176.
[44] M. Mir, N. Ahmed, A.u. Rehman, Recent applications of PLGA based nanostructures in drug delivery, Colloids Surf. B Biointerfaces 159 (2017) 217–231.
[45] F. Sarti, et al., In vivo evidence of oral vaccination with PLGA nanoparticles containing the immunostimulant monophosphoryl lipid A, Biomaterials 32 (16) (2011) 4052–4057.
[46] Q. Wang, et al., Time course study of the antigen-specific immune response to a PLGA microparticle vaccine formulation, Biomaterials 35 (29) (2014) 8385–8393.
[47] C.-N. Njauw, et al., Oncogenic KIT induces replication stress and confers cell cycle checkpoint vulnerability in melanoma, J. Invest. Dermatol. 142 (5) (2022) 1413–1424.e6.
[48] W.-L. Liu, et al., Cytomembrane nanovaccines show therapeutic effects by mimicking tumor cells and antigen presenting cells, Nat. Commun. 10 (1) (2019) 3199.
[49] W.-L. Liu, et al., Expandable immunotherapeutic nanoplatforms engineered from cytomembranes of hybrid cells derived from cancer and dendritic cells, Adv. Mater. 31 (18) (2019) 1900499.
[50] S. Koido, et al., Augmentation of antitumor immunity by fusions of ethanol-treated tumor cells and dendritic cells stimulated via dual TLRs through TGF-β1 blockade and IL-12p70 production, PLoS One 8 (5) (2013) e63498.
[51] W. Song, et al., Enhanced immunotherapy based on photodynamic therapy for both primary and lung metastasis tumor eradication, ACS Nano 12 (2) (2018) 1978–1989.
[52] S.E. Woodman, M.A. Davies, Targeting KIT in melanoma: a paradigm of molecular medicine and targeted therapeutics, Biochem. Pharmacol. 80 (5) (2010) 568–574.
[53] F.S. Hodi, et al., Major response to imatinib mesylate in KIT-mutated melanoma, J. Clin. Oncol. 26 (12) (2008) 2046–2051.
[54] S.H. Robbins, et al., Novel insights into the relationships between dendritic cell subsets in human and mouse revealed by genome-wide expression profiling, Genome Biol. 9 (1) (2008) R17.
[55] R.L. Lindquist, et al., Visualizing dendritic cell networks in vivo, Nat. Immunol. 5 (12) (2004) 1243–1250.
[56] J. Banchereau, R.M. Steinman, Dendritic cells and the control of immunity, Nature 392 (6673) (1998) 245–252.
[57] V. Manolova, et al., Nanoparticles target distinct dendritic cell populations according to their size, Eur. J. Immunol. 38 (5) (2008) 1404–1413.
[58] A.C. Rice-Ficht, et al., Polymeric particles in vaccine delivery, Curr. Opin. Microbiol. 13 (1) (2010) 106–112.
[59] K. Siram, et al., A brief perspective on the diverging theories of lymphatic targeting with colloids, Int. J. Nanomed. 11 (2016) 2867–2872.
[60] S.N. Thomas, A. Schudel, Overcoming transport barriers for interstitial-, lymphatic-, and lymph node-targeted drug delivery, Curr Opin Chem Eng 7 (2015) 65–74.
[61] E. Fröhlich, The role of surface charge in cellular uptake and cytotoxicity of medical nanoparticles, Int. J. Nanomed. 7 (2012) 5577–5591.
[62] X. Chen, et al., Enhanced humoral and cell-mediated immune responses generated by cationic polymer-coated PLA microspheres with adsorbed HBsAg, Mol. Pharm. 11 (6) (2014) 1772–1784.
[63] V. Mulens-Arias, et al., Polyethylenimine-coated SPIONs trigger macrophage activation through TLR-4 signaling and ROS production and modulate podosome dynamics, Biomaterials 52 (2015) 494–506.
[64] S. Pai Kasturi, et al., Prophylactic anti-tumor effects in a B cell lymphoma model with DNA vaccines delivered on polyethylenimine (PEI) functionalized PLGA microparticles, J. Contr. Release 113 (3) (2006) 261–270.
[65] K. Yu, et al., Enhanced delivery of Paclitaxel using electrostatically-conjugated Herceptin-bearing PEI/PLGA nanoparticles against HER-positive breast cancer cells, Int. J. Pharm. 497 (1) (2016) 78–87.
[66] F. Yang, et al., Optimization of critical parameters for coating of polymeric nanoparticles with plasma membrane vesicles by sonication, Sci. Rep. 11 (1) (2021) 23996.
[67] J. Guo, et al., Cancer vaccines from cryogenically silicified tumour cells functionalized with pathogen-associated molecular patterns, Nat. Biomed. Eng. 6 (1) (2022) 19–31.
[68] K. Palucka, J. Banchereau, Cancer immunotherapy via dendritic cells, Nat. Rev. Cancer 12 (4) (2012) 265–277.
[69] V. Subbiah, et al., Cytokines produced by dendritic cells administered intratumorally correlate with clinical outcome in patients with diverse cancers, Clin. Cancer Res. 24 (16) (2018) 3845–3856.
[70] W. Zhang, et al., Tumour necrosis factor-alpha (TNF-alpha) transgene-expressing dendritic cells (DCs) undergo augmented cellular maturation and induce more robust T-cell activation and anti-tumour immunity than DCs generated in recombinant TNF-alpha, Immunology 108 (2) (2003) 177–188.
[71] D. Wohlleber, et al., TNF-induced target cell killing by CTL activated through cross-presentation, Cell Rep. 2 (3) (2012) 478–487.
[72] K.A. Ullrich, et al., Immunology of IL-12: an update on functional activities and implications for disease, Excli j 19 (2020) 1563–1589.
[73] C.T. Hagan, Y.B. Medik, A.Z. Wang, Chapter two - nanotechnology approaches to improving cancer immunotherapy, in: A.-M. Broome (Ed.), Advances in Cancer Research, Academic Press, 2018, pp. 35–56.
[74] Y. Guo, et al., In situ generation of micrometer-sized tumor cell-derived vesicles as autologous cancer vaccines for boosting systemic immune responses, Nat. Commun. 13 (1) (2022) 6534.
[75] A. Schmidt, N. Oberle, P.H. Krammer, Molecular mechanisms of treg-mediated T cell suppression, Front. Immunol. 3 (2012) 51.
[76] A. Verma, et al., T-regulatory cells in tumor progression and therapy, Cancer Manag. Res. 11 (2019) 10731–10747.
[77] S. Chen, et al., Macrophages in immunoregulation and therapeutics, Signal Transduct. Targeted Ther. 8 (1) (2023) 207.
[78] T. Enokida, A. Moreira, N. Bhardwaj, Vaccines for immunoprevention of cancer, J. Clin. Invest. 131 (9) (2021).
[79] Y. Chen, et al., Tertiary lymphoid structures in cancer: maturation and induction, Front. Immunol. 15 (2024).
[80] X.-K. Jin, et al., Engineering metal-based hydrogel-mediated tertiary lymphoid structure formation via activation of the STING pathway for enhanced immunotherapy, Mater. Horiz. 10 (10) (2023) 4365–4379.
[81] M. Chelvanambi, et al., STING agonist-based treatment promotes vascular normalization and tertiary lymphoid structure formation in the therapeutic melanoma microenvironment, Journal for ImmunoTherapy of Cancer 9 (2) (2021) e001906.
[82] R. Cabrita, et al., Tertiary lymphoid structures improve immunotherapy and survival in melanoma, Nature 577 (7791) (2020) 561–565.
[83] M. Meylan, et al., Tertiary lymphoid structures generate and propagate anti-tumor antibody-producing plasma cells in renal cell cancer, Immunity 55 (3) (2022) 527–541.e5.
[84] A. Hennequin, et al., Tumor infiltration by Tbet+ effector T cells and CD20+ B cells is associated with survival in gastric cancer patients, OncoImmunology 5 (2) (2016) e1054598.
[85] S. Gupta, et al., Gender disparity and mutation burden in metastatic melanoma, J. Natl. Cancer Inst.: J. Natl. Cancer Inst. 107 (11) (2015).
[86] T. Steeb, et al., c-Kit inhibitors for unresectable or metastatic mucosal, acral or chronically sun-damaged melanoma: a systematic review and one-arm meta-analysis, Eur. J. Cancer 157 (2021) 348–357.

[87] E.K. Brunsgaard, Y.P. Wu, D. Grossman, Melanoma in skin of color: Part I. Epidemiology and clinical presentation, J. Am. Acad. Dermatol. 89 (3) (2023) 445–456.
[88] E.K. Brunsgaard, J. Jensen, D. Grossman, Melanoma in skin of color: Part II. Racial disparities, role of UV, and interventions for earlier detection, J. Am. Acad. Dermatol. 89 (3) (2023) 459–468.
[89] C. Foged, et al., Particle size and surface charge affect particle uptake by human dendritic cells in an in vitro model, Int. J. Pharm. 298 (2) (2005) 315–322.
[90] M.O. Oyewumi, A. Kumar, Z. Cui, Nano-microparticles as immune adjuvants: correlating particle sizes and the resultant immune responses, Expert Rev. Vaccines 9 (9) (2010) 1095–1107.
[91] A. Sukhanova, et al., Dependence of nanoparticle toxicity on their physical and chemical properties, Nanoscale Res. Lett. 13 (1) (2018) 44.
[92] M. Danaei, et al., Impact of particle size and polydispersity index on the clinical applications of lipidic nanocarrier systems, Pharmaceutics 10 (2) (2018).
[93] T. Fifis, et al., Size-dependent immunogenicity: therapeutic and protective properties of nano-vaccines against tumors, J. Immunol. 173 (5) (2004) 3148–3154.
[94] C. Rolfo, et al., Applications and clinical trial landscape using Toll-like receptor agonists to reduce the toll of cancer, npj Precis. Oncol. 7 (1) (2023) 26.
[95] J.M. Pitt, et al., Targeting the tumor microenvironment: removing obstruction to anticancer immune responses and immunotherapy, Ann. Oncol. 27 (8) (2016) 1482–1492.
[96] Y. Xia, et al., Application of nano-delivery systems in lymph nodes for tumor immunotherapy, Nano-Micro Lett. 15 (1) (2023) 145.
[97] J. Lee, et al., Nanoparticles for lymph node-directed delivery, Pharmaceutics 15 (2) (2023).
[98] L. Zhou, et al., Nano drug delivery system for tumor immunotherapy: next-generation therapeutics, Front. Oncol. 12 (2022) 864301.
[99] L. Liu, et al., Cell membrane coating integrity affects the internalization mechanism of biomimetic nanoparticles, Nat. Commun. 12 (1) (2021) 5726.
[100] R.H. Fang, et al., Cancer cell membrane-coated nanoparticles for anticancer vaccination and drug delivery, Nano Lett. 14 (4) (2014) 2181–2188.
[101] Y. Wang, H. Wang, Lymph node targeting for immunotherapy, Immunooncol Technol 20 (2023) 100395.
[102] R. Yang, et al., Cancer cell membrane-coated adjuvant nanoparticles with mannose modification for effective anticancer vaccination, ACS Nano 12 (6) (2018) 5121–5129.
[103] A.B. Rodriguez, et al., Immune mechanisms orchestrate tertiary lymphoid structures in tumors via cancer-associated fibroblasts, Cell Rep. 36 (3) (2021) 109422.
[104] M.A. Tomai, et al., The immune response modifiers imiquimod and R-848 are potent activators of B lymphocytes, Cell. Immunol. 203 (1) (2000) 55–65.
[105] A. Hargrave, et al., Recent advances in cancer immunotherapy with a focus on FDA-approved vaccines and neoantigen-based vaccines, Vaccines (Basel) 11 (11) (2023).
[106] I. Rastogi, A. Muralidhar, D.G. McNeel, Vaccines as treatments for prostate cancer, Nat. Rev. Urol. 20 (9) (2023) 544–559.
[107] N. Xie, et al., Neoantigens: promising targets for cancer therapy, Signal Transduct. Targeted Ther. 8 (1) (2023) 9.
[108] J.S. Weber, et al., Individualised neoantigen therapy mRNA-4157 (V940) plus pembrolizumab versus pembrolizumab monotherapy in resected melanoma (KEYNOTE-942): a randomised, phase 2b study, Lancet 403 (10427) (2024) 632–644.
[109] V. Shah, et al., Immune checkpoint inhibitors in metastatic melanoma therapy, Med. Int. 4 (2) (2024) 13.
[110] S. Klobuch, et al., Tumour-infiltrating lymphocyte therapy for patients with advanced-stage melanoma, Nat. Rev. Clin. Oncol. 21 (3) (2024) 173–184.
[111] J. Gong, et al., Reversal of tolerance to human MUC1 antigen in MUC1 transgenic mice immunized with fusions of dendritic and carcinoma cells, Proc. Natl. Acad. Sci. U. S. A. 95 (11) (1998) 6279–6283.
[112] Q. Chen, et al., Photothermal therapy with immune-adjuvant nanoparticles together with checkpoint blockade for effective cancer immunotherapy, Nat. Commun. 7 (1) (2016) 13193.
[113] R. Molinaro, et al., Biomimetic proteolipid vesicles for targeting inflamed tissues, Nat. Mater. 15 (9) (2016) 1037–1046.
[114] Q. Ni, et al., A bi-adjuvant nanovaccine that potentiates immunogenicity of neoantigen for combination immunotherapy of colorectal cancer, Sci. Adv. 6 (12) (2020) eaaw6071.